



On the Influence of Large-Scale Atmospheric Motions on Near-Surface Turbulence: Comparison Between Flows Over Low-Roughness and Tall Vegetation Canopies

Sylvain Dupont¹ · Edward G. Patton²

Received: 6 October 2021 / Accepted: 25 April 2022 / Published online: 6 June 2022
© The Author(s), under exclusive licence to Springer Nature B.V. 2022

Abstract

Contrary to Monin–Obukhov similarity theory, near-surface atmospheric turbulence depends not only on local motions but also on larger-scale motions associated with the full atmospheric boundary layer (ABL), where they themselves evolve in character with thermal stratification. After reviewing our current knowledge of ABL motions, we present wavelet velocity and air temperature spectra for both eddy-surface-layer (ESL) flows above rough surfaces and roughness-sublayer (RSL) flows above vegetation canopies, both flows characterizing turbulence over two scales of land roughness. Spectra are extended to the production scale to identify the influence of ABL-scale motions following the thermal stratification. Contrary to turbulence in the ESL, RSL turbulence appears weakly enhanced by ABL-scale motions in near-neutral regimes. With increasing influence of buoyancy, ABL-scale motions play a larger role in ESL and RSL flows, dominating the locally produced turbulence in free convection, while acting to decouple local from the large-scale motions in the stable regime. The behaviour of ESL and RSL spectra with stability variations support the view of, (1) canopy-scale eddies dominating the canopy turbulence over the larger ABL-scale motions in windy conditions, (2) ABL-scale motions known as very-large-scale motions (VLSMs) influencing the ESL horizontal velocity turbulence in windy conditions, and (3) the progressive transitioning of ABL-scale motions from VLSMs to thermals with instability in ESL flows. The direct contribution of ABL-scale motions to near-surface momentum and heat turbulent fluxes appears small. Finally, near-surface velocity spectra are well-approximated as a linear superposition of individual spectra associated to the main eddies populating the flow.

Keywords Atmospheric boundary-layer-scale motions · Atmospheric surface layer · Canopy roughness sublayer · Thermal stability · Wind velocity spectra

✉ Sylvain Dupont
sylvain.dupont@inrae.fr

¹ ISPA, INRAE, Bordeaux Sciences Agro, 33140 Villenave d’Ornon, France

² National Center for Atmospheric Research, Boulder, CO, USA

1 Introduction

In the atmospheric boundary layer (ABL), the near-surface flow is gusty and turbulent in response to the surface friction and heating (or cooling), exhibiting fluctuations from millimetres to several kilometres (Katul 2019). These wind fluctuations play a key role in surface–atmosphere exchanges of mass and energy, in the dispersion of scalars (pollutants, pollen, dust, seeds ...) or trace gases (CO_2), in wind loading on plants and structures such as buildings, bridges or wind turbines, or in wind soil erosion with the suspension of mineral dust in the atmosphere. Understanding the origin of these fluctuations and their distribution in scale is important in identifying the eddy scales involved in the above processes.

By ‘near-surface atmospheric turbulence’, we mean turbulence in the lower atmospheric surface layer (ASL), i.e. within a few metres above rough surfaces, corresponding to the eddy-surface-layer (ESL) turbulence (Hunt and Carlotti 2001; Drobinski et al. 2004) where surface blocking and shear dominate turbulence production, or within a few metres above a vegetation canopy, corresponding to roughness-sublayer (RSL) turbulence (Raupach et al. 1991) where canopy-top Kelvin–Helmholtz instabilities dominate turbulence production (Raupach et al. 1996). See Sect. 2 for a more detailed description of ESL and RSL turbulence. In the lower ASL, near-surface turbulence was first thought to depend only on local properties of the flow, with negligible impact from ABL-scale motions. This represents one of the main hypotheses of the similarity theories developed for near-surface turbulence. However, there has been considerable evidence arising over recent decades showing the influence of ABL-scale motions on near-surface flows (see Sect. 2).

The velocity spectrum represents a classical approach to identifying the impact of ABL-scale motions on near-surface turbulence by looking at the distribution of the velocity fluctuations (variance) as a function of the eddy size (wavenumber or frequency). Above rough surfaces, our knowledge of the form of the velocity spectra and their evolution with thermal stability comes principally from the famous Kansas and Minnesota experiments (Kaimal et al. 1972, 1976), while above vegetation canopies, it comes from several experiments, some of which were compiled in Kaimal and Finnigan (1994), while more recent ones exist, e.g., Su et al. (2004) or Dupont and Patton (2012a). These studies mostly focused on the inertial subrange of the spectrum where the energy cascades from the large-scale anisotropic forcing scale (integral scale) where the fluctuations are produced, to the viscous dissipation scales. For both ESL and RSL flows, the inertial subrange of velocity spectra is usually well-defined with a $-5/3$ power law. Less attention has been devoted to the spectral energy-containing subrange, or the so-called production subrange, where ABL-scale motions may influence fluctuation production. This limited number of studies is explained by the difficulty of extracting low-frequency motions from nonstationary field measurements from a single tower, and the difficulty in simulating the whole spectral range of eddies involved in near-surface turbulence using large-eddy simulation (LES).

Existing studies that focus on the production subrange of the wind velocity spectrum were essentially performed for flows above rough surfaces either focusing on near-neutral stratification (e.g., Katul and Chu 1998; Högström et al. 2002; Mikkelsen et al. 2017) or integrating all stability conditions in order to draw a full-scale spectrum from mesoscale to microscale (e.g., Larsen et al. 2016). Only a few studies focused on partitioning between unstable and stable conditions (McNaughton and Laubach 2000; McNaughton et al. 2007; Zhang et al. 2010; Banerjee et al. 2015; Gao et al. 2016) and only two, to our knowledge, on the difference between ESL and RSL flows but only for near-neutral thermal stratification (Katul et al. 2012; Ghannam et al. 2018). Recently, LES was performed at high spatial

resolution over a rough surface (Salesky and Anderson 2018) and a vegetated canopy (Patton et al. 2016; Perret and Patton 2021), allowing identification of some of the influences of ABL-scale motions on near-surface turbulence for stabilities ranging from neutral to free convection. A clear picture of the sensitivity of the near-surface turbulence to ABL-scale motions, and how the sensitivity evolves with thermal stratification and differs between ESL and RSL flows, is still missing.

The purpose of this study is twofold: first, to review current knowledge of ABL motions and their influence on near-surface turbulence, and second, to explore the impact of ABL-scale motions on turbulence above rough surfaces and above vegetation canopies, and its variability with thermal stratification. Our objectives are (1) to investigate the evolution of ESL and RSL velocity and temperature spectra with stability, from stable to free convection using field measurements, (2) to identify the influence of ABL-scale motions on these spectra according to the thermal stability, and (3) to relate this spectrum sensitivity to thermal stratification to our current understanding of the main coherent motions populating the ABL. The strength of our approach is to perform a wavelet decomposition of the wind velocity and air temperature signals over long periods (> 14 h) in order to discern large-scale (low frequency) motion contributions to the spectra. Prior to presenting the field experiments, we first review our current understanding of near-surface turbulence and motions present in the ABL as they vary with thermal stability, which will serve us in the interpretation of results.

2 Background

The ABL over land is in constant adjustment between the surface radiative heating/cooling, the near-surface ambient wind shear and the entrainment of air from the free troposphere at the top of the ABL, supplemented by secondary forcings such as advection, atmospheric radiation etc. Close to the surface, within the bottom tenth of the ABL, corresponding approximately to the ASL, the flow is mainly influenced by surface friction and heating (or cooling) with a negligible influence of the Earth's rotation (Kaimal and Finnigan 1994). After sunrise, the surface warms up, increasing the instability of the ASL, with the development of a mixed layer above the ASL where large-scale convective motions dominate, while after sunset, the surface radiatively cools down more quickly than the atmosphere aloft, developing a stable boundary layer at the surface, underneath the daytime remaining mixed layer where turbulence decays in the absence of additional production mechanisms (e.g., Darbieu et al. 2015), the so-called residual layer. Under this diurnal pattern, the ABL can be reasonably considered quasi-stationary and in quasi-equilibrium at time scales of about 10–30 min, with continuous turbulence in time and space, with the sunrise and sunset transition periods (Angevine et al. 2020) and very stable conditions (Mahrt 2014) being the exception.

The ASL is divided into two layers: in the lower part, either the ESL above low-roughness elements such as sand surfaces, grass fields, water bodies (referred hereafter as rough surfaces), or the RSL in the presence of tall roughness elements such as trees, buildings (referred hereafter as canopies), and the inertial sublayer (ISL) above. Unlike the RSL, the ESL is not as well established for describing the lower ASL above low-roughness surfaces. The notion of an ESL comes from the phenomenological idea of Hunt and Morrison (2000) that when contacting the surface, the impinging large-scale motions develop an internal boundary layer at the surface in which small eddies develop, similar to wake motions shed by roughness elements (Högström et al. 2002). In the ESL, the surface blocking and shear induced by impinging large-scale motions are the dominant mechanisms producing turbulence (Hunt

and Carlotti 2001). The depth of this layer depends on the character of the underlying surface, but can extend vertically from the surface by as much as one-tenth of the ASL, i.e. about 10 m (Hunt and Carlotti 2001). In the RSL, the flow is also under the influence of the individual roughness element wakes, but in a closer vicinity to the roughness elements than in the ESL as the turbulent flow extends within the canopy, i.e. between the roughness elements. Momentum is not only absorbed at the ground surface as in ESL flows but is also absorbed through the whole canopy depth. In RSL flow, Kelvin–Helmholtz instabilities at the canopy top induced by the inflection point in the mean velocity profile is the dominant mechanism producing turbulence, which produces canopy-scale eddies similar to coherent mixing-layer type eddies (Raupach et al. 1996). The RSL depth is about two to five times the roughness element height, including the canopy (Raupach et al. 1991). In the ISL above, the mean flow has equilibrated with the turbulence produced by the surface roughness elements, is horizontally homogeneous, and is well represented by similarity theory. By analogy with laboratory wall bounded-shear flow, the ASL could be referred to as the inner layer and the mixed/residual layers as the outer layer, except that the scale separation between inner and outer layer is notably wider in the ABL than in the laboratory.

2.1 A Local View of the Near-Surface Turbulence

The main characteristics of ASL flow over flat uniform surfaces (wind and scalar profiles, fluxes) have been described by Monin–Obukhov similarity theory (MOST, Monin and Obukhov 1954), which hypothesizes that turbulent flow and transport in the ASL depends mainly on local eddies, whose length scales with the distance z from the surface, and whose velocity scales with the surface friction velocity u_* ($= \sqrt{\tau_w/\rho}$, with τ_w the surface shear stress and ρ the air density) characterizing the momentum absorbed by the surface.

In MOST, thermal stratification effects on the mean velocity and scalar profiles are only accounted for by adjusting the near-neutral turbulent eddy diffusivity of momentum and scalar using similarity universal functions determined empirically from experimental datasets. These universal functions depend only on one dimensionless stability parameter z/L , where L is the Obukhov length (Obukhov 1946). This length characterizes the height above which buoyant production (or destruction) dominates wind-shear production of turbulent kinetic energy. The Obukhov length L depends only on four local parameters: z , u_* , the surface kinematic heat flux H , and the buoyancy parameter g/T_v , where g is the acceleration due to gravity and T_v is the reference virtual temperature: $L = -u_*^3 T_v / (\kappa g H)$ with κ the von Kármán constant. The sign of L reflects the direction of the heat flux, negative for diurnal unstable conditions with an upward heat flux, and positive for nocturnal stable conditions with a downward heat flux. In near-neutral conditions, thermal stratification is negligible and $|L| \rightarrow \infty$.

In the vicinity of a dense canopy, the flow's momentum is primarily absorbed through the canopy depth, vertically displacing the mean height at which momentum is absorbed from the ground surface in ESL flows to the so-called displacement height d in RSL flows (Kaimal and Finnigan 1994). In addition to the shear-surface-layer-type eddies scaling here with the distance $z - d$, larger canopy-scale eddies are also generated by the velocity inflection-point instability present at canopy top (Raupach et al. 1996; Katul and Chang 1999). Their presence invalidates MOST in the RSL, as demonstrated by observing larger vertical fluxes than the local gradient should support (Denmead and Bradley 1987). Corrections to MOST have been proposed for the RSL by accounting for an additional length scale characterizing

the mixing-layer type eddies, the vorticity thickness of the flow at canopy top (Harman and Finnigan 2007, 2008; Finnigan et al. 2009).

For both the ESL and the RSL flows, the important hypothesis of MOST and RSL-corrected MOST, respectively, is the negligible influence of large ABL-scale motions. Although MOST has been relatively well verified above uniform surfaces for wind velocity profiles, scalar properties, and momentum and scalar fluxes (Kaimal and Finnigan 1994), and RSL-corrected MOST as well over several canopies (Harman and Finnigan 2007, 2008; Weligepolage et al. 2012; Shapkalijevski et al. 2016), large scatter in similarity universal functions has been reported; scatter not solely attributable to random errors, which suggests a need for additional nondimensional parameters to represent additional physical processes not considered in MOST (e.g. Salesky and Chamecki 2012). In fact, growing evidence suggests ABL-scale motion influence on near-surface flows, which means that the fit of the similarity universal functions with field data to account for thermal stratification, may unknowingly integrate some of the ABL-scale motion influence, explaining some of the observed scatter in similarity universal functions.

2.2 Influence of ABL-Scale Motions on Near-Surface Turbulence

The influence of large-scale motions on near-surface turbulence has been the subject of extensive research, initially through laboratory studies of boundary-layer flows. Townsend (1961) first hypothesized that near-wall flow consists of ‘active’ and ‘inactive’ motions. Active motions correspond to locally produced eddies, scaling with z and u_* , producing the shear stress, which are well represented by MOST for atmospheric flows, while inactive motions correspond to ABL-scale eddies that augment the variance of the near-wall horizontal flow velocity but not the near-wall shear stress. Townsend’s hypothesis has been supported by several laboratory experiments (Bradshaw 1967; Antonia and Raupach 1993) showing substantial variance at low frequency in the near-surface horizontal velocity spectra, scaling with the boundary-layer depth instead of z . Evidence supporting this role of inactive motions in near-wall turbulence often hinges on the presence of a k^{-1} region within the energy-containing subrange of horizontal velocity spectra, where k is the wavenumber. This k^{-1} scaling was first theorized by Tchen (1953) based on a spectral budget. Then, other theories were proposed based on asymptotic matching between scalings of locally-generated eddies and large-scale eddies (Perry et al. 1986; Kader and Yaglom 1991; Nickels et al. 2005), superposition of eddy cascades generated at all possible distances from the surface (Nikora 1999), a unified theory between Tchen’s spectral budget, Nikora’s (1999) phenomenological theory and Heisenberg’s (1948) eddy viscosity (Katul et al. 2012), or a dimensional analysis of the joint probability density function of multipoint velocity differences, resulting from a generalization of MOST based on two dimensionless length scales, the traditional vertical scale $-z/L$ and an additional horizontal eddy scale $-k/L$ (Tong and Nguyen 2015).

In the atmosphere, the influence of ABL-scale motions on near-surface turbulence was also observed in horizontal wind velocity spectra, with a spectral peak shifting to lower frequencies with increasing instability, without scaling with z (Kaimal et al. 1972). The results of Kaimal et al. (1972) for the daytime horizontal velocity variance represented one of the community’s first hints at MOST’s failure (Kaimal and Finnigan 1994). Because this departure from MOST was only observed in daytime unstable conditions, this was attributed to the influence of convective motions from the mixed layer above. This led Kaimal (1978) and Højstrup (1982) to represent the horizontal velocity spectrum in the ASL as a linear superposition of a surface-layer spectrum corresponding to MOST and a mixing-layer spectrum scaling

with the ABL depth, where the first spectrum represents the locally produced eddies and the second represents the large-scale convective eddies aloft. This picture, however, does not explain the influence of ABL-scale motions in neutral stratification observed in laboratory experiments (Bradshaw 1978).

The influence of ABL-scale eddies on near-neutral ASL turbulence was later confirmed by observing an extended energy-containing subrange in near-surface horizontal velocity spectra containing a low-frequency region matching k^{-1} scaling (Katul and Chu 1998; Drobinski et al. 2004; Calaf et al. 2013; Banerjee et al. 2015), or equivalently by observing a logarithmic scaling in the production subrange of the second-order horizontal velocity structure function (Chamecki et al. 2017; Ghannam et al. 2018). Similar scaling was also recently observed in an ASL air temperature spectrum (Li et al. 2016). However, k^{-1} scaling for velocity spectra is not systematically observed. The energy containing subrange of Kaimal et al.'s (1972) spectra did not exhibit a k^{-1} scaling in near-neutral conditions. Morrison et al. (2002) argued against its existence. Nickels et al. (2005) suggested that the existence of the k^{-1} scaling depends on the measurement height as compared to the surface roughness and boundary-layer depth, the measurement height modulating the scale separation between the local and large-scale eddies. We suspect that the absence of k^{-1} scaling in Kaimal et al.'s (1972) spectra could be explained by, (1) that Kaimal et al. (1972) ensemble-averaged observations obtained over a large depth of the ASL (over heights ranging from 4 to 32 m) to produce their normalized spectra, or (2) that Kaimal et al. (1972) focused primarily on the inertial subrange of the spectra, hence their spectra were limited in their low-frequency extent.

In the ESL, this influence of ABL-scale motions on near-neutral surface turbulence is suspected to result from the impingement of large-scale eddies onto the ground (Hunt and Graham 1978; McNaughton and Laubach 2000; Hunt and Carlotti 2001; Högström et al. 2002; Zhang et al. 2010). The blockage by the surface of the downwelling portion of ABL-scale motions stretches them along the mean wind direction through pressure redistribution converting downward vertical motions into horizontal motions, leading to elongated stream-wise structures at the surface, with longitudinal scale larger than z . This explains the observed extra low-frequency energy of the horizontal wind velocity spectrum as opposed to the vertical wind velocity spectrum. This could also explain the juxtaposed meandering regions of low- and high-speed streaks near the surface (Drobinski et al. 2004), although these large-scale spanwise variations of the mean velocity could as well result from shear-instabilities induced from irregular distribution of surface roughness elements (e.g., Reynolds et al. 2007; Vanderwel and Ganapathisubramani 2015).

In the RSL, the impact of large-scale eddies on the canopy flow has been less investigated as most studies focused on the mixing-layer type eddies. Raupach et al. (1996) first suspected that the impingement of large-scale eddies onto canopies may enhance locally wind shear at the canopy top, triggering the canopy-scale eddies. A k^{-1} scaling in the canopy-top horizontal wind velocity spectrum and its equivalent logarithmic scaling in the velocity structure function have been reported in near-neutral conditions from field experiments by Katul et al. (2012) and Ghannam et al. (2018), and from LES results of Pan and Chamecki (2016), suggesting an influence of ABL-scale motions, but this scaling extended in wavenumber over less than a decade. Patton et al.'s (2016) LES results did not show a k^{-1} scaling law in neutral condition at canopy top (deduced from their Fig. 8 showing two-dimensional (2D) spectra), but did show k^{-1} scaling at twice the height of the canopy. However, their LES results suggested that ABL-scale motions organize exchanges at canopy top, showing a two-way coupling between ABL-scale and canopy-scale motions (Patton et al. 2016; Perret and Patton 2021). In convective conditions, Dupont and Patton (2012a, b) suspected from the Canopy Horizontal Array Turbulence Study (CHATS) experiment an influence of ABL-scale

downward convective plumes on the canopy flow statistics as these motions penetrate within the canopy. This was confirmed later by Patton et al. (2016)'s LES results with an extended energy-containing subrange of the canopy-top horizontal velocities, scaling with the ABL depth and with a power law between -1 and $-5/3$ (their Fig. 8).

The spatial character of the ABL-scale motions evolves with changes in atmospheric stability (e.g., Moeng and Sullivan 1994; Khanna and Brasseur 1997; Sullivan et al. 2016) which alters the spectral subrange in both the ESL and RSL as the near-surface turbulence adjusts to the evolution of the energy-containing large-scale turbulence. This adjustment has been rarely presented from field experiments. To our knowledge, only Banerjee et al. (2015) have shown a progressive transition of the scaling law from -1 to $-5/3$ with increasing stability over a uniform surface. In stable conditions, a gap between local and large-scale eddies is suspected, which would limit the influence of ABL-scale motions on local turbulence. McNaughton and Laubach (2000) observed a such a gap in spectra collected above a paddy field downwind of an extensive dry region (corresponding to a turbulent stable layer beneath a convective layer), and by Cheynet et al. (2018) over a marine atmospheric boundary layer.

2.3 Near-Surface Turbulent Transport by ABL-Scale Motions

The contribution of ABL-scale motions to near-surface momentum and scalar turbulent transports is usually considered negligible near the surface. Following Townsend's (1961) hypothesis, large-scale motions are largely 'inactive' at transporting momentum (or scalar) compared to local 'active' motions, which suggests that large-scale motions only perturb the turbulent transport without altering the total exchange at the surface. The contribution of large-scale motions to the momentum-scalar transport only becomes significant at large distance above the surface, because the vertical velocity component associated with these large-scale motions is small compared to their horizontal velocity components. This interpretation is justified by the apparent insensitivity of near-surface momentum cospectra and vertical velocity spectra to large-scale motions (e.g., Bradshaw 1967; Antonia and Raupach 1993; Katul et al. 1996; Katul and Chu 1998; McNaughton and Laubach 2000). However, several studies have reported significant contribution of large-scale motions to the near-wall momentum transport (e.g., Ganapathisubramani et al. 2003; Guala et al. 2006; Lee and Sung 2011).

This confusion surrounding the role of ABL-scale motions in near-surface turbulent transport could potentially be reconciled if the large ABL-scale motions alter or influence the small-scale motions performing the transport. Counter to Townsend's (1961) hypothesis that the large-scale motions do not interact with the smaller near-surface scale motions, it seems that large-scale motions actively modulate the amplitude and frequency of near-surface small-scale fluctuations (Mathis et al. 2009; Baars et al. 2015; Salesky and Anderson 2018; Perret and Patton 2021) and therefore may organize the spatial distribution or modulate the production of active sweep and ejection motions transporting momentum, as observed at canopy top from LES results of Patton et al. (2016).

2.4 Evolution of ABL-Scale Motions with Varying Stability and Potential Influence on ASL Motions

To understand how the influence of ABL-scale motions on near-surface turbulence changes with thermal stratification, it is important to have an understanding of the coherent motions present in the ABL. Since the last decades, we now better understand the turbulent coherent

structures present in the ABL and their evolution with thermal stability. This was made possible thanks to field observations (e.g., Lemone 1973; Wilczak and Tillman 1980; Atkinson and Zhang 1996; Weckwerth et al. 1997) and LES performed from neutral to free convection regimes over rough and vegetated surfaces (e.g., Deardorff 1972; Moeng and Sullivan 1994; Brasseur and Wei 1994; Finnigan et al. 2009; Bailey and Stoll 2016; Patton et al. 2016; Salesky et al. 2017; Salesky and Anderson 2018; Jayaraman and Brasseur 2021; Perret and Patton 2021).

In neutrally-stratified channel flows, the elementary coherent structures populating the surface-shear flow are downstream head-up hairpin vortices resulting from the upward stretching of spanwise vortices. These hairpin vortices occur in streamwise succession,

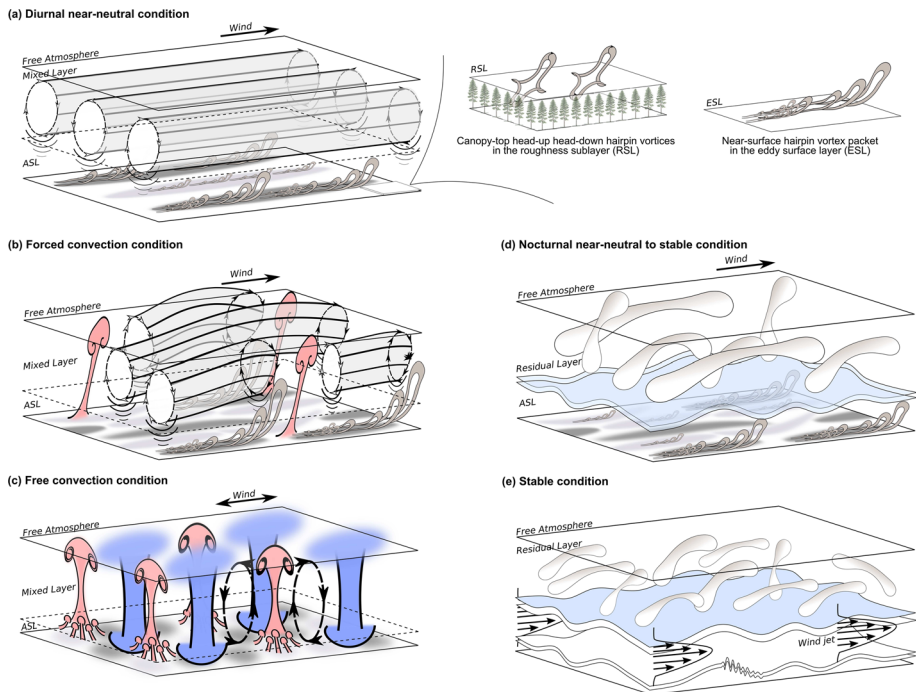


Fig. 1 Idealized schematic of the main coherent motions present in the ABL according to the thermal stratification. **a** The diurnal near-neutral condition is characterized by longitudinal high- and low-speed streaks (VLSMs) in the ASL, combined with convective rolls within the mixed-layer above. Near the surface (right figure), head-up head-down hairpin vortices dominate the turbulence at canopy top (RSL flow) while head-up hairpin vortex packets (LSMs) dominate above rough surfaces (ESL flow). **b** Forced convection is intermediate between diurnal near-neutral (**a**) and free convection (**c**) conditions, with an increasing inclination of the ASL hairpin vortices toward the vertical before ultimately forming plumes that disturb the convective rolls. **c** Free convection conditions are characterized near the surface by rising plumes of warm air that merge into large-scale thermals (updrafts), compensated by large-scale downdrafts of cool air. Near the surface, patches of local wind shear form between the convergence/divergence regions induced by these large-scale updrafts and downdrafts. **d** The nocturnal near-neutral to stable condition is characterized by a progressive decoupling with increasing stability between the near-surface turbulence and the above residual layer, reducing the influence of ABL-scale motions on near-surface turbulence, and thus reducing the size of the longitudinal streaks (VLSMs). **e** The stable condition is characterized by a decoupling between the near-surface layer and the above decaying residual layer. Near the surface the turbulence is intermittently missing, perpetuated by sporadic bursts from, for example, residual-layer motions, a low-level jet, or gravity waves. See Sect. 2.4 for more details

so-called hairpin vortex packets (see the right schematic of Fig. 1a), with size increasing downstream (Adrian 2007). Compared to surface-shear flows dominating the ESL, in the RSL the wind shear peaks at canopy top, which leads to the development of downstream head-up ejection-generating hairpin vortices, paired with upstream head-down sweep-generating hairpin vortices (Finnigan et al. 2009). The head-up structure is stretched upward by the flow, ensuring a progressive transition with the overlying ISL where the flow behaves like a surface-shear flow, while the downward progression of the head-down structures is constrained by both the canopy drag and the surface (see the middle schematic of Fig. 1a). The mechanism by which canopy-scale coherent structures transition to surface-shear flow structures with increasing height above the canopy remains poorly constrained.

In the ABL, these near-surface hairpin vortex structures are embedded within a larger environment containing ABL-scale structures as well, with a larger separation of scales between inner (active) and outer (inactive) motions than in laboratory. The ABL eddy structures also evolve continuously with variations in the thermal stratification in response to the balance between buoyancy- and shear-driven turbulence production. However, the hierarchical relationship among these structures of varying scale, e.g. top-down versus bottom-up mechanism of formation, is still in debated (e.g., Fesquet et al. 2009). Figure 1 proposes a schematic describing the evolution of these structures and their interactions according to the thermal stability.

- Daytime near-neutral regime (Fig. 1a): this regime is often referred to as a moderately convective regime (Khanna and Brasseur 1998; Jayaraman and Brasseur 2021) as it is characterized by significant wind speed and small positive surface heat flux. The dominant wind shear within the ASL produces above surface roughness elements packets of head-up hairpin vortices, also known as large-scale motions (LSMs), that scale with the ASL depth and carry most of the turbulent kinetic energy and momentum of the ASL. These LSMs align to form very large-scale elongated meandering regions of low- and high-speed streaks, the so-called very-large-scale motions (VLSMs), that scale with more than 10 times the ASL depth (Kim and Adrian 1999; Hutchins and Marusic 2007; Marusic and Monty 2019). Large-eddy simulations of ABL flows have shown the influence of VLSMs on the near-surface turbulence (Salesky and Anderson 2018; Perret and Patton 2021), as observed above rough surfaces from laboratory experiments and direct numerical simulation (e.g., Marusic and Hutchins 2008; Mathis et al. 2009). For this regime, the k^{-1} scaling law at production scales of the horizontal wind velocity spectrum of ESL flows is often thought to result from the overlapping of two energy distributions, one associated with the LSMs and the other with the VLSMs (Kim and Adrian 1999). Above the ASL, the mixed layer is dominated by longitudinal convective rolls aligned along the mean wind direction (Lemone 1973; Moeng and Sullivan 1994). It is believed that the ASL shear-driven motions are somehow linked to these mixed-layer convective rolls. Khanna and Brasseur (1998) argued that buoyancy-driven upwelling motions emanate from the warm surface along the ASL low-speed streaks where the wind shear is weak. These buoyant plumes concentrate into elongated sheets that drive the vertical component of the large-scale longitudinally-aligned convective rolls in the mixed layer. The initiation of this coupling between the ASL longitudinal streaks (VLSMs) and mixed-layer convective rolls was numerically observed by Jayaraman and Brasseur (2021) in a canonical daytime ABL, starting however from a stability critical state too close to the theoretical neutrality regime to be observable in real ABL over a steady-state regime. Other mechanisms may trigger mixed-layer convective rolls such as an inflection point in the wind profile of the

- Ekman layer, gravity waves in the free atmosphere, among others (Atkinson and Zhang 1996; Young et al. 2002).
- Nocturnal near-neutral to stable regime (Fig. 1d): this regime corresponds to the weakly stable regime defined by Mahrt (2014). The still fully turbulent condition of this regime leads to ASL turbulence structures similar as during the daytime near-neutral regime. For this regime, numerical simulations have shown the presence within the ASL of numerous vertically-extent warm-cool temperature fronts, whose inclination increases with stability. The cool fronts appear associated to head-up vortices while the warm fronts are more likely associated to either head-down or ring vortices (Gerz et al. 1994; Sullivan et al. 2016). As the stable stratification increases above the surface roughness elements, the ASL turbulent motions decouple progressively from the above residual layer ones as well as from those inside the canopy as the thermal stratification often remains unstable there. The decoupling between near-surface and large-scale motions might reduce the size of VLSMs since the ABL depth becomes progressively a less relevant length scale. With lower influence of ABL-scale motions, in this regime, the ASL longitudinal velocity variance may be reasonably well represented by MOST (RSL-corrected MOST) in ESL (RSL) flows.
 - Free convection regime (Fig. 1c): the concomitant large heat flux from the surface or canopy and low wind speed leads to rising plumes of warm air in the ASL that merge into narrow and intense large-scale thermals in the mixed layer. These thermals are organized into open cells similar to turbulent Rayleigh–Bénard convection in laboratory flow, with large but weaker downdrafts in the middle of the cells. In the presence of a canopy, the penetration of large-scale downdrafts within the canopy is attenuated through momentum absorption as these large-scale motions encounter the canopy elements (Dupont and Patton 2012b). In this regime, the local shear-driven turbulence occurs primarily between the near-surface regions of large-scale convergence and divergence, produced beneath the large-scale updrafts and downdrafts. Consequently, the near-surface wind velocity field is characterized by patches of low and high wind speed. In ESL flows, the ASL depth can be as low as a few metres deep (McNaughton 2004).
 - Forced convection regime (Fig. 1b): this regime is intermediate between the daytime near-neutral and the free convection regimes. The LES results of Salesky and Anderson (2018) revealed that with increasing instability, the ASL hairpin vortices above roughness elements progressively tilt upward before ultimately forming plumes, inducing a progressive transitioning from convective rolls to thermals in the mixed layer, as the thermally driven instabilities start to fully dominate the wind shear instabilities within the ASL. Near the surface, it is not clear whether there is a distinct superposition of shear- and buoyantly-driven motions, or if shear-driven motions become progressively buoyantly-driven motions (Dupont and Patton 2012b). For simplicity, this intermediate regime is thought as a mix of left-over rolls and rising thermals, with more inclined hairpin vortices and smaller VLSMs in the ASL than in the daytime near-neutral regime.
 - Very stable regime (Fig. 1e): this regime occurs preferentially before sunrise under weak geostrophic wind forcing and clear sky. The low turbulence production by the weak ambient wind shear cannot counterbalance the turbulence destruction by the strong radiative surface cooling, making the usual partitioning in layers of the ABL inadequate (Mahrt 2014). In this regime, the size of the eddies are more constrained by the stratification than by their distance to the ground (displaced ground in presence of canopy), making MOST (RSL-corrected MOST) inapplicable. The near-surface flow is globally intermittent, i.e. with periods where turbulent motions of all size are intermittently missing (van de Wiel et al. 2012; Mahrt 2014), perturbed by sporadic bursts from mesoscale motions,

residual-layer motions, elevated-shear-layers (low-level jet) motions, or within-canopy thermal plumes, generating instabilities or gravity waves.

This discussion suggests that variations in the structure of large ABL-scale turbulence with bulk atmospheric stability might impact the character of near-surface turbulence. From our perspective, VLSMs and thermals appear to be the most likely large-scale motions influencing near-surface turbulence; VLSMs under windy near-neutral conditions and thermals under convective conditions.

3 Materials and Methods

This section describes a range of field campaign datasets and the techniques by which those datasets are interrogated toward identifying the role and impact of large-scale motions on near-surface turbulence.

3.1 Field Experiments

Five field experiments were selected in order to interrogate turbulence over a variety of surface-roughness characteristics, ranging from bare soil, sparsely vegetated surface, no-leaf orchard, with-leaf orchard, to a maritime pine forest, and allowing to investigate both ESL and RSL flows. These five experiments are as follows. Table 1 summarizes their main characteristics.

- Bare soil (WIND-O-V17): The WIND-O-V’s 2017 field campaign (Dupont et al. 2018, 2019) took place in South Tunisia on the experimental range (Dar Dhaoui, 33°17’45’’ N, 10°46’57’’ E) of the Institut des Régions Arides (IRA) of Médenine close to Médenine/Zarzis. The site approximates a flat half-circle plot of 150-m radius where measurements were performed at the centre of the circle in order to ensure a fetch of at least 150 m for northerly winds. The plot surface was bare soil with a low roughness length, around 10^{-4} m, as deduced from the wind velocity profile (Dupont et al. 2018). The three velocity components (u , v , w , referring to the longitudinal, lateral and vertical velocity components, respectively) and air temperature (θ) were measured at four heights (1.0, 1.9, 3.0 and 4.1 m), using four three-dimensional (3D) ultra sonic anemometers (one

Table 1 Experimental characteristics: measurement heights used in this study (z), vegetation canopy height (h), displacement height (z_d), sampling frequency (f), time period duration used to perform the wavelet transform after removing the border effects, and Nb is the number of events

Experiment	z (m)	h (m)	z_d (m)	f (Hz)	Duration (h)	Nb
WIND-O-V17	1.0, 1.9, 3.0*, 4.1	–	0.0	60, 50, 50, 20	15	11
WIND-O-V18	1.0, 1.9, 3.0*, 4.1	0.14	0.0	60, 50, 50, 20	15	22
CHATS-noleaves	10.0*, 29.0	10.0	5.8	60	15	11
CHATS-leaves	10.0*, 29.0	10.0	7.8	60	15	18
PIN	9.85*, 14.15	8.4	5.9	20	25	18

z_d is negligible for surfaces with low roughness elements while z_d was estimated from within-canopy momentum flux profiles in near-neutral conditions for the CHATS experiments, and was simply estimated as $0.7h$ for the PIN experiment

*Reference height

Campbell Scientific CSAT3, two Gill R3, and one Gill WindMaster) sampling at 60, 50, 50 and 20 Hz, respectively. Measurements were recorded from March 1 to May 15 2017, allowing sampling over a large range of thermal stratifications, including several aeolian soil erosion events.

- Sparsely vegetated soil (WIND-O-V18): On the same site as the WIND-O-V17 experiment, a second campaign was performed in 2018 with the same experimental set-up but the plot was covered with thousands of 0.4 m high barley (*Hordeum vulgare*) tufts, regularly arranged, about 3.3 m apart, covering less than 2% of the plot, and leading to a roughness length of about 3×10^{-3} m.
- Walnut orchard without leaves (CHATS-noleaves): The CHATS experiment took place on a 0.64 km² walnut (*Juglans regia*) orchard block located on a flat terrain in Dixon, California (USA). The experiment is documented in Patton et al. (2011), the statistical analysis of the wind dynamics over the walnut canopy are described in Dupont and Patton (2012a, b), and we used here version 2 of the dataset (Horst 2019). A first intensive measurement period was conducted before the walnut trees leafed out. The trees were all about 10 m high and the cumulative plant area index (PAI) was about 0.7. Among other measurements, turbulent velocity components were measured simultaneously at six levels within the canopy (1.5, 3.0, 4.5, 6.0, 7.5, 9.0 m), one at canopy top (10.0 m), and six levels above the canopy (11.0, 12.5, 14.0, 18.0, 23.0, 29.0 m) using Campbell Scientific CSAT3 sonic anemometers sampling at 60 Hz. For this study, we only focus on measurements at canopy top (10.0 m) and at the highest level (29.0 m).
- Walnut orchard with leaves (CHATS-leaves): During the CHATS experiment, a second intensive measurement period was performed after leaf-out of the walnut trees with the same experimental set-up. The PAI was about 2.5, with a lower density in the subcanopy.
- Pine forest canopy (PIN): The wind velocity and the air temperature were measured during the summer and autumn 2016 over a maritime pine (*Pinus pinaster* Ait.) forest (Dupont et al. 2020). The forest plot was located at the Salles Integrated Carbon Observation Station (ICOS) (44°29' N, 0°57' W), in Les Landes region, in southwestern France. The forest plot covered about 0.23 km² and was characterized by a mean tree height of $h = 8.4$ m and a PAI of about 3.5. The ground surface was flat in all directions, and the forest was wide enough to have negligible fetch effect in all wind directions (fetch ranging from 275 to 350 m long). The three velocity components and air temperature were measured at three heights (2.9, 9.85 and 14.15 m), using three 3D ultra sonic anemometers (two Gill R3, and one Gill WindMaster) sampling all at 20 Hz. Here, we only focus on measurements above the canopy (9.85 and 14.15 m).

For all sites, the surrounding environment (i.e. several kilometres around the site) was relatively homogeneous over a flat terrain, corresponding to a composite of bare soils with small bushes or olive-tree plots for the WIND-O-V experiments, a mix of different walnut and almond orchard blocks for the CHATS experiment, and a mix of crop and maritime pine forest plots for the PIN experiment.

For each experiment, we define ‘events’ as long time periods (19- to 29-h) within our sampled time series that satisfy the following three criteria: (1) contiguously available data, (2) consistent wind spectra over 30-min windows along the long time periods (visual inspection), and (3) relatively stationary wind direction from that with the largest fetch, i.e. northerly winds for the WIND-O-V experiments, southerly winds for the CHATS experiments, and all wind directions for the PIN experiment. Note that for ABL-scale motions, the size of the fetch is not critical as these motions are larger than the instrumented plot. Atmospheric-boundary-layer-scale motions are more likely influenced by the whole regional environment of the

plot than by the plot itself. Characteristics describing each of the selected events (long-time periods) are presented in the Online Resource Tables S1–S5.

Such long-time periods include low-frequency fronts related to changing mesoscale weather patterns as well as diurnally varying winds and temperature. Fortunately, shifts in the mesoscale weather patterns occurred at distinctly lower frequencies (with time scales ranging from several hours to a few days) compared to the ABL-scale motions (with ≈ 10 – 15 min time scales) with clear separation in energy spectra, allowing us to distinguish ABL-scale motions from mesoscale patterns in velocity and temperature spectra (see Sects. 4.1 and 4.2).

To account for any potential imperfection in the orientation of the sonic anemometers during deployment, the planar-fit method proposed by Wilczak et al. (2001) was applied on the velocity components of all experiments. Then, the recorded velocity components were rotated horizontally so that the instantaneous longitudinal velocity (u) represents the horizontal component in the primary wind direction along a centred 2-h period. This moving 2-h period over each data point was preferred to the usual every 30-min period in order to observe the low-frequency behaviour (fluctuation periods shorter than 2 h) of the transverse wind velocity spectra.

3.2 Wavelet Spectra and Cospectra

To detect low-frequency motions on the near-surface turbulence, wavelet decompositions of the three velocity components and air temperature were performed. The wavelet technique has been extensively used in atmospheric science (Domingues et al. 2005), leading to wavelet spectra with analogous scaling to usual Fourier spectra (e.g., Katul and Parlange 1994, 1995). Unlike the Fourier transform, the wavelet transform unfolds turbulent variable time series into both time and scale, allowing retention of information on the time variation of the signal (Torrence and Compo 1998); where retention of time information is achieved from the convolution of the signal with a wavelet function well defined-in-time and frequency as opposed to a convolution with a periodic sinusoidal function only localized in frequency for the Fourier transform. This latter signal decomposition using infinite sinusoidal functions explains why application of the Fourier transform requires stationarity of the signal, while the signal decomposition using finite in time wavelet functions makes the wavelet transform applicable to nonstationary times series (Schaller et al. 2017). Hence, as in Dupont (2020), wavelet decompositions over long duration (several hours) enable estimating the low-frequency contribution (fluctuation periods larger than 30 min) to shorter time resolution (30 min) velocity and temperature variances, and momentum and heat fluxes.

Here, the wavelet decompositions were obtained over 15- to 25-h long time series after removing any border effects, delimited by the so-called cone of influence, which varies solely with the scale of the wavelet (Torrence and Compo 1998). The complex-valued Morlet wavelet ($\Psi_0(t) = \pi^{-1/4} e^{i\omega_0 t} e^{-t^2/2}$), with the nondimensional frequency $\omega_0 = 6$ was used because of its relatively good resolution in both time and frequency. Then, the wavelet spectra and cospectra were estimated every 30 min along these 15- to 25-h time periods, by integrating the wavelet transform scalogram over each 30-min period. This approach allowed us to include in the 30-min average spectra and cospectra, the contributions from motions with larger time scales than 30 min. This 30-min period represents the approximate turnover time of largest eddies in the ABL under convective conditions and hence the typical duration considered for ASL turbulence statistics.

3.3 Ensemble Average

Spectra and cospectra were ensemble-averaged according to the atmospheric stability of the 30-min periods in order to investigate how they evolve with thermal stratification. Atmospheric stability was defined by $(z - z_d)/L$ evaluated at a reference height, where z_d is the displacement height (see Table 1). The reference height was the canopy top h for the CHATS and PIN experiments and 3 m above the ground for the WIND-O-V experiments. We defined eight stability regimes that were delineated according to the behaviour of the 30-min average friction velocity (u_*), sensible heat flux (H_{sens}), skewness of the vertical wind velocity (Sk_w) and correlation coefficient for momentum (r_{uw}) as a function of $(z - z_d)/L$ (Fig. 2), all estimated at the reference height. Compared to Dupont and Patton (2012a), we added three stability regimes (1) by separating the near-neutral regime according to the sign of the heat flux to determine whether the influence of ABL-scale motions on near-surface turbulence changes as the sign of the heat flux switches while the mean wind intensity remains similar, (2) by splitting the free convection regimes into two in order to better identify the transition of the wind spectra with increasing instability, and (3) by adding a very stable regime.

The four stability regimes in unstable conditions have been defined as follows with increasing instability:

- Diurnal near-neutral (referred hereafter as NN+): in this regime, the momentum flux is significant and the heat flux is small and positive, toward the atmosphere. This regime occurs mostly during windy and/or cloudy days, or to a lesser degree during sunrise. The difference in u_* between experiments (Fig. 2) reflects first the roughness of the surface, i.e. its capacity to absorb momentum, where canopy flows often exhibit larger u_* than low-roughness surface flows, and second the synoptic wind intensity during the selected periods. Canopy flows (CHATS and PIN) exhibit larger r_{uw} than does the bare-surface flow (WIND-O-V17), about 0.45 and 0.25, respectively; and, the sparsely-vegetated-surface flow (WIND-O-V18) is intermediate with $r_{uw} = 0.30$. This difference in r_{uw} between the ESL and RSL flows is in agreement with the literature (Kaimal and Finnigan 1994) and reflects the increased efficiency of momentum transport produced by the coherent mixing-layer type structures at canopy top. For the same reasons, Sk_w exhibit larger negative values at canopy top than near the surface, reflecting the intermittent penetration of canopy-top eddies within the canopy.
- Forced convection (FoC): here, the heat flux is positive and large and the momentum flux is significant, resulting from large mean wind speeds, but often not as high as in the NN+ regime. This regime occurs mostly during the day, and especially in the afternoon. In this regime, r_{uw} exhibits the same magnitude as in the NN+ regime, suggesting eddies of similar type dominate the turbulence. However, Sk_w increases near smooth surfaces, reaching values near zero, while Sk_w remains similar as the NN+ regime for the canopies cases.
- Transition to free convection (tFrC): this regime is characterized by a significant positive heat flux, and a reduced momentum flux compared to the FoC regime. For all cases, r_{uw} decreases with increasingly negative $(z - z_d)/L$ and Sk_w increases, with values becoming positives for ESL flows. This indicates a change in the character of the turbulence structures.
- Free convection (FrC): here, the heat flux is positive, not necessarily high, and the momentum flux is small, associated with light wind speeds. This regime mostly occurs during the day, especially in the morning. Here, r_{uw} is low and Sk_w reaches a new equilibrium

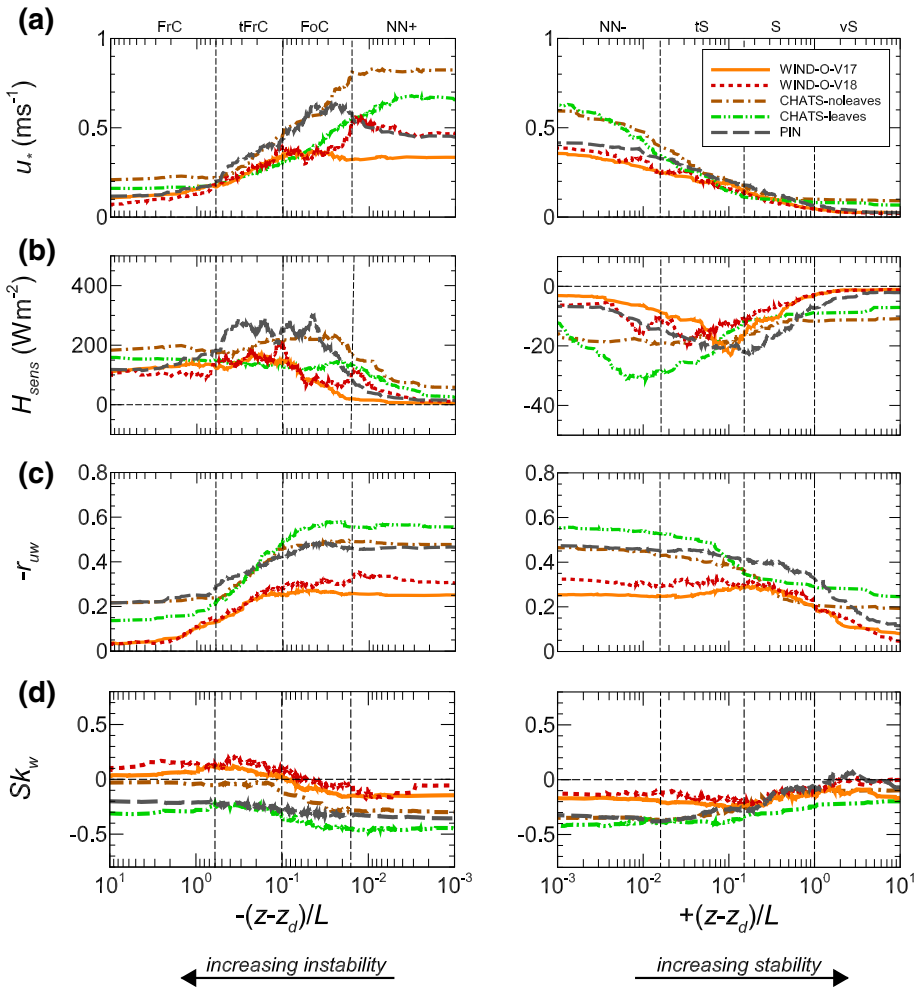


Fig. 2 **a** Friction velocity u_* , **b** sensible heat flux H_{sens} (where $H_{sens} = \rho c_p H$ and c_p is the specific heat at constant pressure), **c** correlation coefficient for momentum $-r_{uw}$, and **d** skewness of the vertical velocity component Sk_w , as a function of $(z - z_d)/L$, at the reference height (Table 1) for all experiments. The dashed vertical lines delineate the stability regimes: free convection (FrC), transition to free convection (tFrC), forced convection (FC), diurnal near-neutral (NN+), nocturnal near-neutral (NN-), transition to stable (tS), stable (S), and very stable (vS). Curves were obtained from a running average of $(z - z_d)/L$ over all 30-min values from each experiment

with $-(z - z_d)/L$, with low negative values for the PIN and CHATS-leaves canopies, near zero for the CHATS-noleaves canopy, and positive values for smooth surfaces.

The four stability regimes in stable conditions have been defined as follows with increasing stability:

- Nocturnal near-neutral (NN-): in this regime, the main characteristics of the wind dynamics are similar as in the NN+ regime, except that the heat flux is negative (Fig. 2). This regime occurs mostly during windy nights or at sunset.

- Transition to stable (tS): This regime occurs during the night with moderate wind conditions. In this regime, the absolute value of the heat flux reaches a maximum, and r_{uw} and Sk_w are similar in magnitude as in the NN–regime.
- Stable (S): This regime occurs at night with weak, but finite wind speeds. The amplitude of the heat flux decreases with increasing $(z - z_d)/L$, as buoyancy inhibits vertical exchange. The value of r_{uw} also decreases with increasing $(z - z_d)/L$, especially for canopy cases.
- Very stable (vS): In this regime, the heat flux is negative and the momentum flux is small resulting from light winds. This regime occurs mostly just before sunrise.

For each experiment, Table 2 summarizes the total number of 30-min periods considered in our analysis for each of the above stability regimes. Online Resource Tables S6–S10 provide a breakdown of the number of 30-min periods for each stability class identified within each of the events used in this study. Although identifying the long events required wind directions with the largest fetch, any 30-min period within each of these events and falling outside this requirement were discarded from the ensemble average.

3.4 Spectral Decomposition

In order to evaluate the contribution from large-scale motions on the near-surface wind velocity and air temperature fluctuations, we assume that the spectra can be represented as a linear superposition of individual spectra scaling with the main eddies present in the flow. This linear composition of velocity spectra is in line with previous works, e.g., (1) the proposition of Kaimal (1978) and Højstrup (1982) for convective conditions that velocity spectra are the linear composition/superposition of spectra of local eddies scaling with z and of large-scale eddies scaling with the ABL depth, (2) the observation by Kim and Adrian (1999) that the near-wall longitudinal velocity spectrum has a bimodal distribution whose components are associated with LSM and VLSM, and (3) the suggestion of Nikora (1999) in neutral conditions that velocity spectra are the superposition of spectra of all eddies larger than z .

Hence, we query whether the velocity and air temperature spectra S_i normalized by their respective variance σ_i can be represented as the superposition of p individual spectra (spectral modes) scaling with the main eddies producing turbulence near the surface. Here, i refers either to u , v , w or θ . This leads to:

Table 2 Number of 30-min periods considered in each stability regime in our analysis for each experiment: very stable (vS); stable (S); transition to stable (TS); nocturnal near-neutral (NN–); diurnal near-neutral (NN+); forced convection (FC); transition to free convection (tFrC); free convection (FrC)

Experiment	Stable				Unstable				Total
	vS	S	tS	NN–	NN+	FoC	tFrC	FrC	
WIND-O-V17	3	6	17	19	26	105	78	33	287
WIND-O-V18	1	3	25	12	32	212	184	38	507
CHATS-noleaves	2	34	55	27	31	35	33	6	224
CHATS-leaves	4	12	58	105	102	90	48	18	437
PIN	97	200	112	55	32	225	153	26	900

The event periods considered in each experiment is detailed in Online Resource Tables S1–S10

$$\frac{kS_i}{\sigma_i} = \sum_p \alpha_{ip} S(k, k_{0,ip}), \tag{1}$$

where k is the wavenumber, $k_{0,ip}$ is a fitting parameter related to the wavenumber at the spectral peak ($k_{m,ip}$), S is the individual form of a premultiplied spectrum normalized by its variance, and $\alpha_{ip} = a_{ip} / \sum_p a_{ip}$ represents the contribution of the spectrum $S(k, k_{0,ip})$ where a_{ip} is a fitting parameter. Hence, α_{ip} represents the contribution of each spectral mode to the time-series variance. The form of S corresponds to that which one usually considers for stable conditions (Kaimal and Finnigan 1994), which should not be influenced by LSMs, viz.,

$$S(k, k_0) = \frac{0.164 (k/k_0)}{1 + 0.164 (k/k_0)^{5/3}}, \tag{2}$$

where k_0 corresponds to $k_{0,ip}$ in Eq. 1, i.e. the wavenumber where the extrapolated inertial subrange line of the p^{st} spectral mode of variable i reaches $S = 1$. The wavenumber k_0 is related to the spectral peak wavenumber k_m as $k_m \approx 3.8k_0$ (Kaimal and Finnigan 1994).

4 Results

4.1 Wind Velocity Spectra

Figures 3 and 4 present ensemble-averaged premultiplied wavelet spectra of the three wind velocity components (u , v , and w), obtained for one ESL flow (WIND-O-V17) and one RSL flow (CHATS-leaves), respectively, for all stability regimes and measurement heights. Spectra from the other experiments exhibit for all stability classes similar differences to those found between these RSL and ESL flows, therefore, the spectra from the other experiments are only presented in Online Resource Figs. S1–S3. In all figures, Taylor’s frozen turbulence hypothesis has been invoked to convert time to length scales, which assumes that all eddies advect at the streamwise mean velocity component. Although velocity fluctuations at canopy top are of the similar order as the mean wind speed, the validity of Taylor’s hypothesis still remains acceptable because the dominant eddies at canopy top travel at substantially higher speeds than the local mean wind speed (Zhang et al. 1992; Kaimal and Finnigan 1994; Shaw et al. 1995). The streamwise wavenumber was estimated as $k = 2\pi/\lambda$, where the wavelength λ was approximated by u/f , with f the frequency and u the mean streamwise velocity component at height z . In the figures, k is normalized by z .

In both ESL and RSL flows, the velocity spectra exhibit at high wavenumbers the expected inertial subrange with a $k^{-2/3}$ scaling ($k^{-5/3}$ in non-premultiplied spectra) for all stability regimes, except in the vS regime for the PIN experiment due to weak turbulence. At low wavenumbers ($kz < 0.001 - 0.005$ in ESL flows and $kz < 0.04 - 0.1$ in RSL flows), daytime u -spectra generally present a spectral gap, i.e. a minimum between two spectral peaks, separating 3D boundary-layer turbulence (high wavenumbers) from the 2D mesoscale motions (low wavenumbers). These latter motions are typically related to frontal passages. Note that the v -spectra have been shortened at low wavenumbers (periods larger than 2 h) to remove their fall-off resulting from the rotation performed on the horizontal velocity components, that produced zero mean v for periods larger than 2 h. The primary differences in the wind spectra between ESL and RSL flows and between stability regimes, occurs at medium wavenumbers where the variance is produced.

Near-neutral nighttime (NN– regime) and daytime (NN+ regime) wind spectra do not present significant differences in ESL and RSL flows. The ESL u - and v -spectra exhibit a

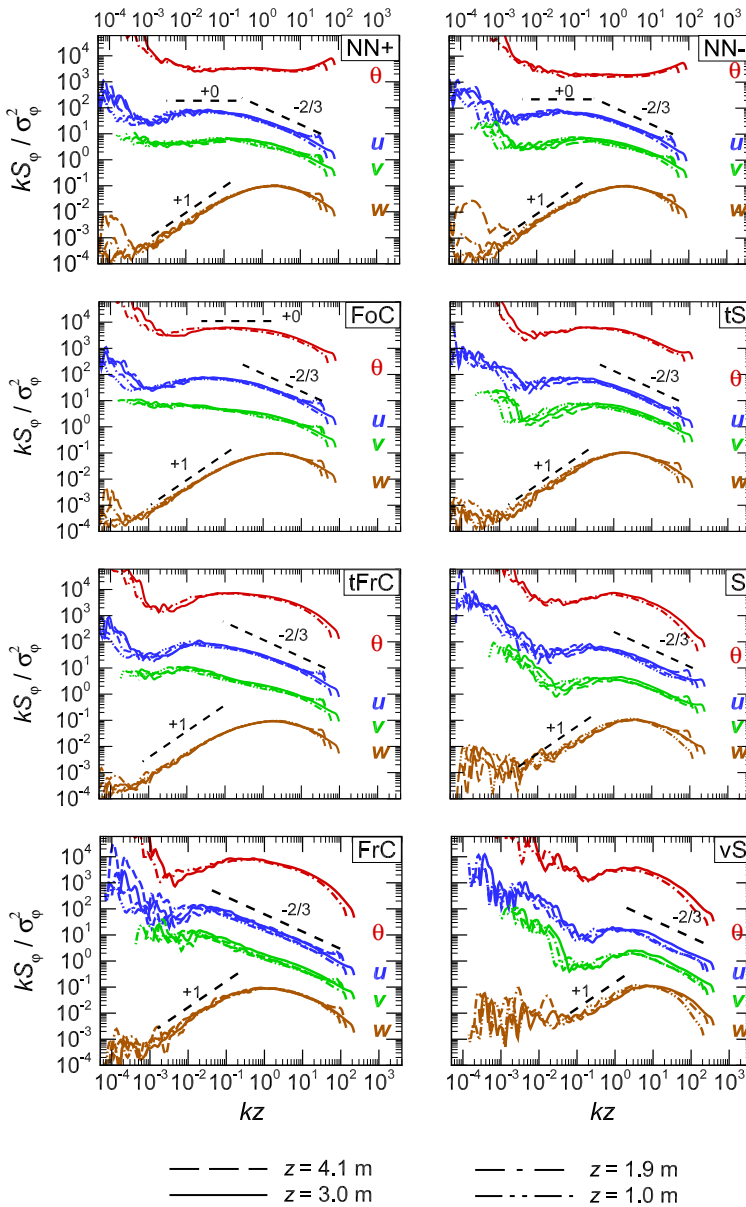


Fig. 3 Ensemble-averaged wavelet-based 30-min pre-multiplied energy spectra of the streamwise velocity (S_u , blue), spanwise velocity (S_v , green), vertical velocity (S_w , brown) components, and air temperature (S_θ , red) at the four measurement heights of the WIND-O-V17 experiment. The spectra are normalized by the variance σ_ϕ^2 of the considered quantity ϕ . The wavenumber k was deduced as $k = 2\pi f/u$, where f is the frequency and u the mean wind speed at the measurement height, and was normalized by the measurement height z . Spectra are shifted upward or downward to permit comparison. Air temperature spectra at 1.0 and 4.1 m heights were discarded because the former exhibited damped temperature fluctuations at high frequencies, and the latter had too many erratic values. Similarly, velocity spectra at 4.1 m heights in vS regimes were discarded because of too many erratic values. An equivalent figure for the WIND-O-V18 experiment is available in Online Resource Fig. S1

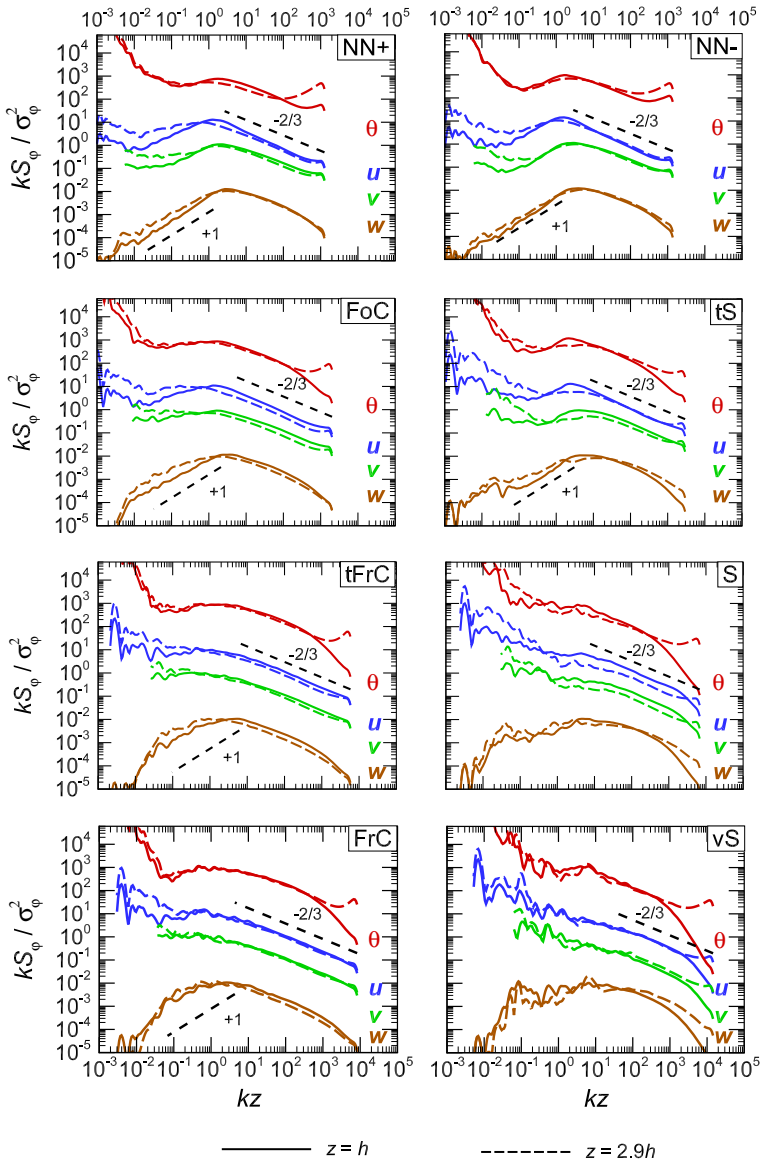


Fig. 4 Ensemble-averaged wavelet-based 30-min pre-multiplied energy spectra of the streamwise velocity (S_u , blue), spanwise velocity (S_v , green), vertical velocity (S_w , brown) components, and air temperature (S_θ , red) for the CHATS-leaves experiment at canopy top and at $z = 2.9h$. The spectra are normalized by the variance σ_ϕ^2 of the considered quantity ϕ . The wavenumber k was deduced as $k = 2\pi f/u$, where f is the frequency and u the mean wind speed at the measurement height, and was normalized by the measurement height z . Spectra are shifted upward or downward to permit comparison. Equivalent figures for the CHATS-noleaves and PIN experiments are available in Online Resource Figs. S2 and S3

plateau (k^0) at mid-wavenumbers, corresponding to the k^{-1} scaling often reported in the literature in non-premultiplied spectra (see Sect. 2.2). This plateau covers one decade, between $10^{-2} \leq kz \leq 10^{-1}$. Without normalizing k by z (not shown), the position of this plateau remains constant with the measurement height, suggesting that this plateau is mostly influenced by motions with length scales larger than the measurement height, i.e. ABL-scale motions. Unlike the u - and v -spectra, the premultiplied w -spectra exhibit a marked peak, followed by a well-defined k^{+1} scaling on its low-wavenumber side. This w -spectrum peak is also located at higher wavenumbers ($kz = 2$) than where the premultiplied u - and v -spectrum plateau, and scales with z , suggesting that motions of size z are the main contributors to the w variance. The RSL spectra exhibit marked peaks for the three velocity components, at about $kz = 1.5$ for u , 2.0 for v , and 3.5 for w , flanked at canopy-top by a k^{+1} scaling in the production subrange, and a slightly lower scaling above the canopy, suggesting a larger contribution from large-scale motions. The RSL u - and v -spectrum peaks are also closer to the w -spectrum peak than in the ESL flows, which indicates that structures are not as longitudinally extensive in RSL flows compared to ESL flows.

With increasing instability, the ESL near-neutral plateau (k^0 scaling) of the u - and v -spectra progressively inclines toward the $-2/3$ slope of the spectrum inertial subrange, reflecting a larger contribution of the low-wavenumber motions to u and v variances. In the FrC regime, this leads to a long inertial subrange extending from $kz = 0.05$ to 10^2 with $k^{-2/3}$ scaling. A similar behaviour is observed in RSL flows, where the $+1$ slope of the near-neutral production subrange of the u - and v -spectra levels off with instability to reach a plateau (k^0 scaling) in the FrC regime for the CHATS experiments, or even further to a near $-2/3$ slope for the PIN experiment. For w -spectra, the $+1$ slope of the near-neutral production subrange levels off as well for RSL flows, indicating more energy at low wavenumbers. This is not observed for the ESL flows, where the w -spectra do not change much with increasing instability, except a small shift of its peak toward lower wavenumbers.

In stable conditions, the spectral gap observed in unstable conditions at low-wavenumbers shifts to higher wavenumbers with increasing stability, and also appears in the w -spectra. This gap could suggest a decoupling between the near-surface turbulence and the overhead motions likely connected with the residual layer of the diurnal mixed layer. In the S and vS regimes, the w -spectrum flattens as the turbulence decreases, especially in RSL flows, while the u - and v -spectra still show a $-2/3$ region, except for the PIN experiment.

4.2 Air Temperature Spectra

Figures 3 and 4 show also the wavelet-based air temperature (θ) spectra. As for the velocity spectra, the daytime θ -spectra exhibit a gap at low wavenumbers, separating 3D turbulence from near-2D mesoscale motions, except in near-neutral conditions for ESL flows. This gap is located at higher wavenumbers than for the velocity spectra for conditions other than free convection and stable, suggesting a larger influence of mesoscale fluctuations. This might result from entrainment of warm air occurring at the ABL-top capping inversion.

In near-neutral conditions, the ESL θ -spectra are relatively flat from mid to high wavenumbers, demonstrating no clear scale within this band acting as a source of temperature fluctuations because the surface acts as neither a significant heat source nor a heat sink. At high wavenumbers, θ -spectra exhibit positive slopes near $+1$, which is characteristic of white noise suggesting that the temperature variance is too small compared to the instrument noise. For this regime, the main source of temperature fluctuations comes from mesoscale motions (low wavenumbers). The RSL θ -spectra are less flat, probably due to the unstable

conditions prevailing within the canopy; they resemble the u -spectra but with white noise at high wavenumbers.

With increasing instability (FoC to FrC regimes), a plateau (k^0) emerges at mid-wavenumbers in the ESL θ -spectra at an intermediate scale between the u - and w -spectrum peaks, while the RSL θ -spectrum peaks are more easily identified and are located at scales similar to those in the u -spectrum. In both ESL and RSL flows, the θ -spectra do not show a well-defined $k^{-2/3}$ scaling at high wavenumbers, but present some curvature. This curvature could either suggest a continuous production of θ variance across a range of scales instead of only a transfer of energy from mid to small scales as in the u -spectrum inertial subrange, or could result from the spatial attenuation of θ -fluctuations at high wavenumbers due to path-averaging between the sonic anemometer transducers (attenuation that is usually more pronounced in temperature spectra than in wind spectra; Horst and Oncley 2006).

In stable regimes, the spectral gap shifts to mid-wavenumbers in ESL flows ($\approx 0.2kz$) as in u - and v -spectra, decoupling the near-surface temperature fluctuations from the large-scale temperature fluctuations. In RSL flows, the separation between near-surface and large-scale temperature fluctuations is not as clear. For both ESL and RSL flows, the θ -spectrum inertial subrange does not scale well with $k^{-2/3}$.

4.3 Large-Scale Contribution

The velocity and air temperature spectra at 3 m height above the rough surfaces in the ESL flows and at canopy top in the RSL flows are fit with a linear superposition of individual spectra (spectral modes) associated to different eddy scales to create a multimodal distribution (Sect. 3.4), neglecting the mesoscales. Only daytime conditions are considered, i.e. from NN+ to FrC regimes, because the influence of ABL-scale motions on near-surface turbulence is less significant at night (stable conditions). Our goal is to identify the main eddy scales contributing to the velocity and air temperature variances.

The fitting procedure was performed starting with three spectral modes, whose spectral peak wavenumbers $k_{m,ip}$ (as a reminder, p refers to the mode number from 1 to 3, starting at low wavenumbers, and i to either u , v , w or θ) were constrained in the following variation ranges: $0.004 \leq k_{m,i1} < 0.06$, $0.06 \leq k_{m,i2} < 2$ and $2 \leq k_{m,i3} < 4$ for ESL flows, and $0.04 \leq k_{m,i1} < 0.8$, $0.8 \leq k_{m,i2} < 80$ and $80 \leq k_{m,i3} < 10^3$ for RSL flows. These ranges cover the peaks or bumps observed in the spectra. Then, the modes with proportion rate (α_{ip} in Eq. 1) lower than 0.1 for all unstable regimes were removed from the fit, reducing the number of modes included.

Overall, ESL and RSL spectra are reasonably well described by two spectral modes, except for the ESL u - and v -spectra where three spectral modes were required. Only the ESL θ -spectra in near-neutral regimes (NN+) could not be fitted due to the low spectral energy from mid to high wavenumbers. As an example, Figs. 5 and 6 illustrate the nice fit of the velocity and air temperature spectra obtained for the WIND-O-V17 and CHATS-leaves experiments. Figures presenting data from other experiments are available in Online Resource Figs. S4–S6.

Figures 7 and 8 present the peak wavenumber ($k_{m,ip}$) and contribution of the spectral modes (α_{ip}) (left and right figures, respectively) as a function of the atmospheric thermal stability $[(z - z_d)/L]$ for the ESL and RSL flows, respectively. For both flows, the highest-wavenumber spectral mode ($p = 3$ for ESL flows and $p = 2$ for RSL flows) peaks around $k_{m,ip}z = 1 - 5$. This mode corresponds to local eddies scaling around z and is that usually represented by MOST and the RSL corrected-MOST, respectively. The lowest-wavenumber spectral mode ($p = 1$) peaks around $k_{m,i1}z = 0.005 - 0.04$ in ESL flows and around

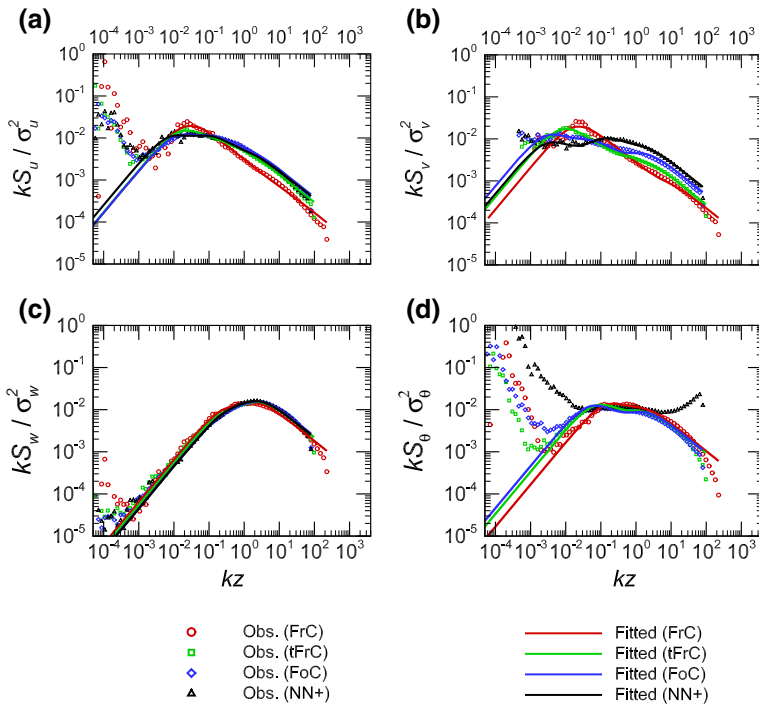


Fig. 5 Ensemble-averaged wavelet-based 30-min premultiplied energy spectra (symbols) of the streamwise velocity S_u (a), spanwise velocity S_v (b), vertical velocity S_w (c), and air temperature S_θ (d) at 3 m height for the WIND-O-V17 experiment and for the four unstable regimes: free convection (FrC), transition to free convection (tFrC), forced convection (FC), diurnal near-neutral (NN+). The spectra are normalized by the variance σ_φ^2 of the considered quantity φ . The wavenumber k was deduced as $k = 2\pi f/u$, where f is the frequency and u the mean wind speed at the measurement height, and was normalized by the measurement height z . Curves represent fitted spectra resulting from the linear superposition of individual spectra whose peak wavenumber and contribution rate are presented in Fig. 7. Mesoscale contributions to the spectra were not considered in the fitting procedure. For S_θ (d), no fitted spectrum was obtained for the NN+ regime due to the low high-frequency energy of θ fluctuations for this stability regime. An equivalent figure for the WIND-O-V18 experiment is available in Online Resource Fig. S4

$k_{m,i}z = 0.05 - 0.8$ in RSL flows. For ESL flows, this mode corresponds to ABL-scale motions of about 1800m (wavelength $\lambda_{m,ip} = 2\pi/k_{m,ip}$), while for RSL flows this mode appears associated to smaller motions (about 315 m scale). This scale difference likely reflects having used velocity at canopy-top to relate observed frequency and wavenumber in the RSL flows compared to having used velocity well above the roughness elements in ESL flows; due to their vertical extent and invariance of their length scale with height, canopy-scale eddies in RSL flows are thought to convect at speeds consistent with wind speeds at heights more like $z = 2h$ (e.g., Zhang et al. 1992; Shaw et al. 1995). The intermediate-wavenumber spectra mode ($p = 2$) of the ESL u - and v -spectral peaks around $k_{i2}z = 0.1 - 0.8$, and corresponds to eddy sizes of about 100m, which is of the same order as the generally considered depth of the ASL in presence of wind.

In ESL flows, the u - and v -spectra appear dominated in near-neutral conditions by the two large-scale modes ($p = 1$ and $p = 2$) that contribute to 90% of the u -spectrum (Fig. 7a, right panel) and 80% of the v -spectrum (Fig. 7b, right panel), while the local-scale

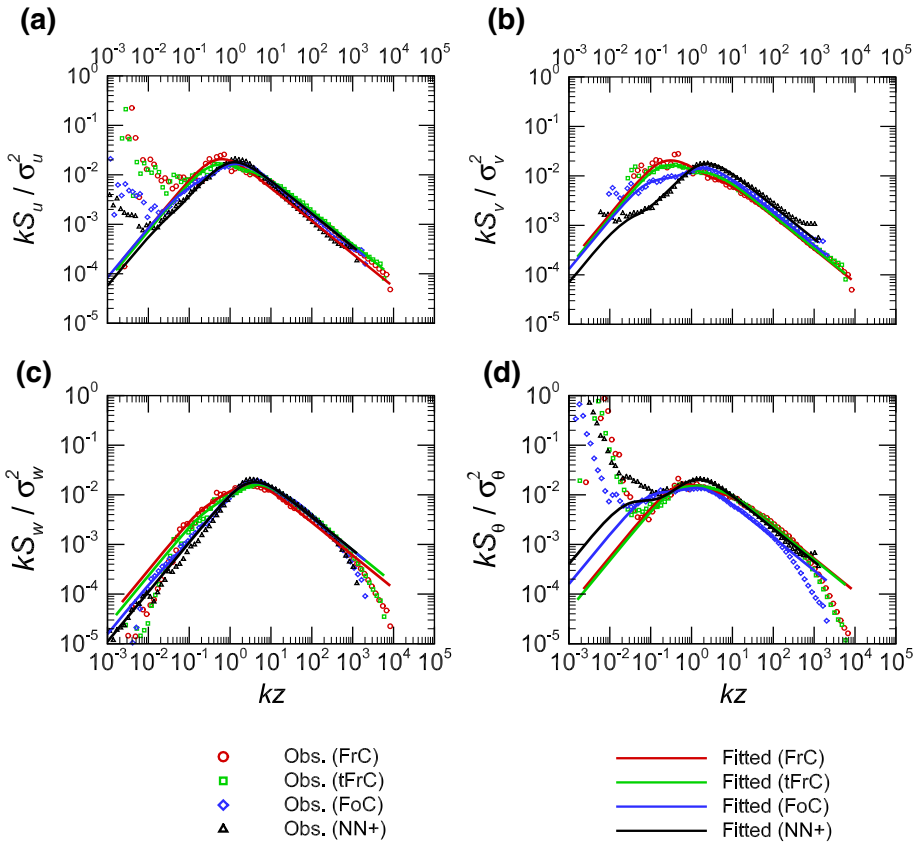


Fig. 6 Ensemble-averaged wavelet-based 30-min premultiplied energy spectra (symbols) of the streamwise velocity S_u (a), spanwise velocity S_v (b), vertical velocity S_w (c), and air temperature S_θ (d) at canopy top for the CHATS-leaves experiment and for the four unstable regimes: free convection (FrC), transition to free convection (tFrC), forced convection (FC), diurnal near-neutral (NN+). The spectra are normalized by the variance σ_φ^2 of the considered quantity φ . The wavenumber k was deduced as $k = 2\pi f/u$, where f is the frequency and u the mean wind speed at the measurement height, and was normalized by the measurement height z . Curves represent fitted spectra resulting from the linear superposition of individual spectra whose peak wavenumber and contribution rate are presented in Fig. 8. Mesoscale contributions to the spectra were not considered in the fitting procedure. Equivalent figures for the CHATS-noleaves and PIN experiments are available in Online Resource Figs. S5 and S6

mode ($p = 3$) contributes to approximately 70% of the w -spectra (Fig. 7c, right panel). This result is consistent with the plateau observed on u - and v -spectra (k^{-1} scaling in non-premultiplied spectra), which is usually associated to LSMs. Among the two large-scale modes, the intermediate mode ($p = 2$) represents about 50% (40%) and the largest mode ($p = 1$) about 40% (40%) of the u (v) variance, respectively. The peaks of these two large-scale modes delimit the plateaus of the u and v spectra. With increasing instability, the contribution from the largest-scale mode increases in u and v variances, with especially large increases occurring at around $-(z - z_d)/L \approx 0.05$ (FoC regime), while the contribution from the intermediate- and lowest-scale modes diminishes. This transition reflects the level-off of the u and v -spectra at low wavenumbers, transitioning from k^0 (plateau) to $k^{-2/3}$ scaling, suggesting a larger-contribution of ABL-scale motions to the u - and v -variances.

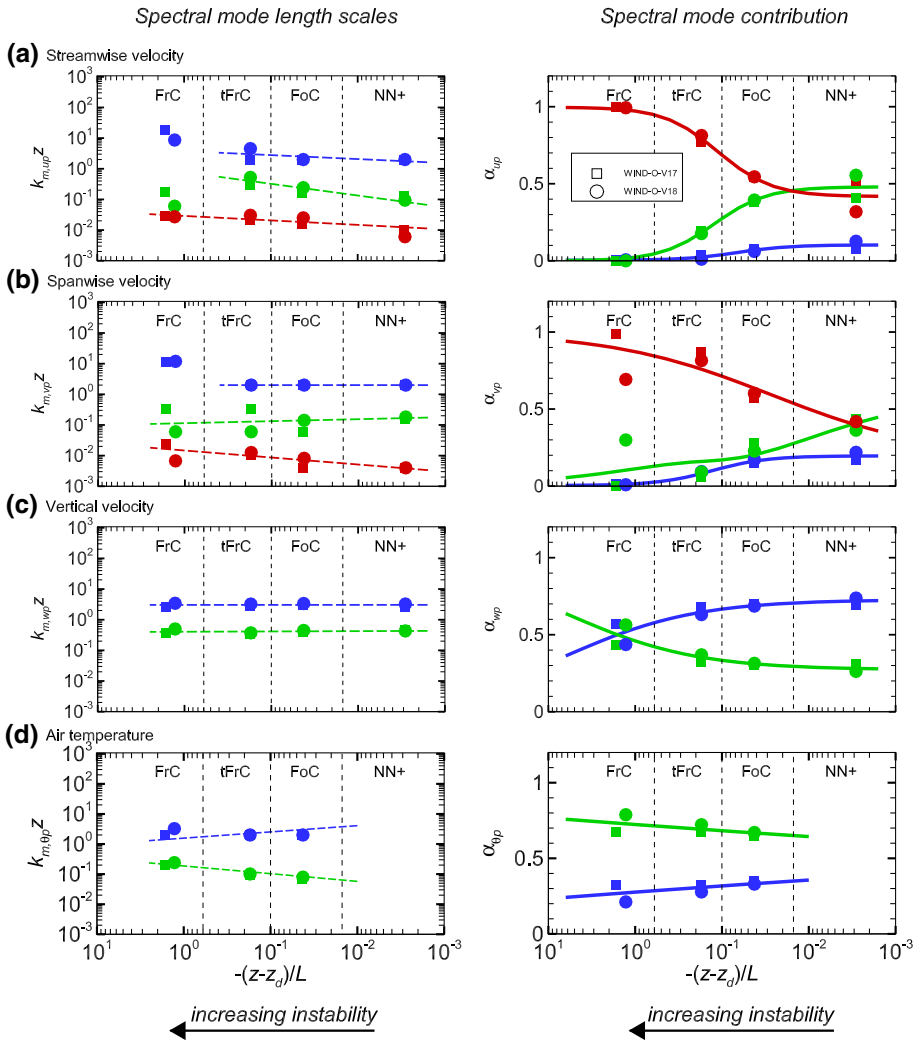


Fig. 7 Characteristics of the spectral modes used to fit spectra of the 3-m high streamwise velocity (a), spanwise velocity (b), vertical velocity (c), components and air temperature (d), as a function of $-(z - z_d)/L$, obtained for the ESL flows (WIND-O-V17 and WIND-O-V18 experiments) in unstable conditions [$(z - z_d)/L < 0$]. The fitted spectra were obtained from the linear superposition of three individual spectra for the horizontal wind velocity components ($p = 1$ (red), 2 (green) and 3 (blue)) and two spectra for the vertical wind velocity component and the air temperature ($p = 2$ (green) and 3 (blue)). The peak wavenumbers ($k_{m,ip}$) and proportion rates (α_{ip}) of spectral modes are presented on the left and right figures, respectively. The dashed lines on the left figures are a linear fit in the log–log plot of the spectrum peak wavenumbers as a function of $-(z - z_d)/L$ without considering the points whose spectral mode proportion rate α_{ip} is zero, and the curves on the right figures represent a fit of the spectrum proportion rate as a function of $-(z - z_d)/L$. The dashed vertical lines delimit the stability regimes: free convection (FrC), transition to free convection (tFrC), forced convection (FC), and diurnal near-neutral (NN+)

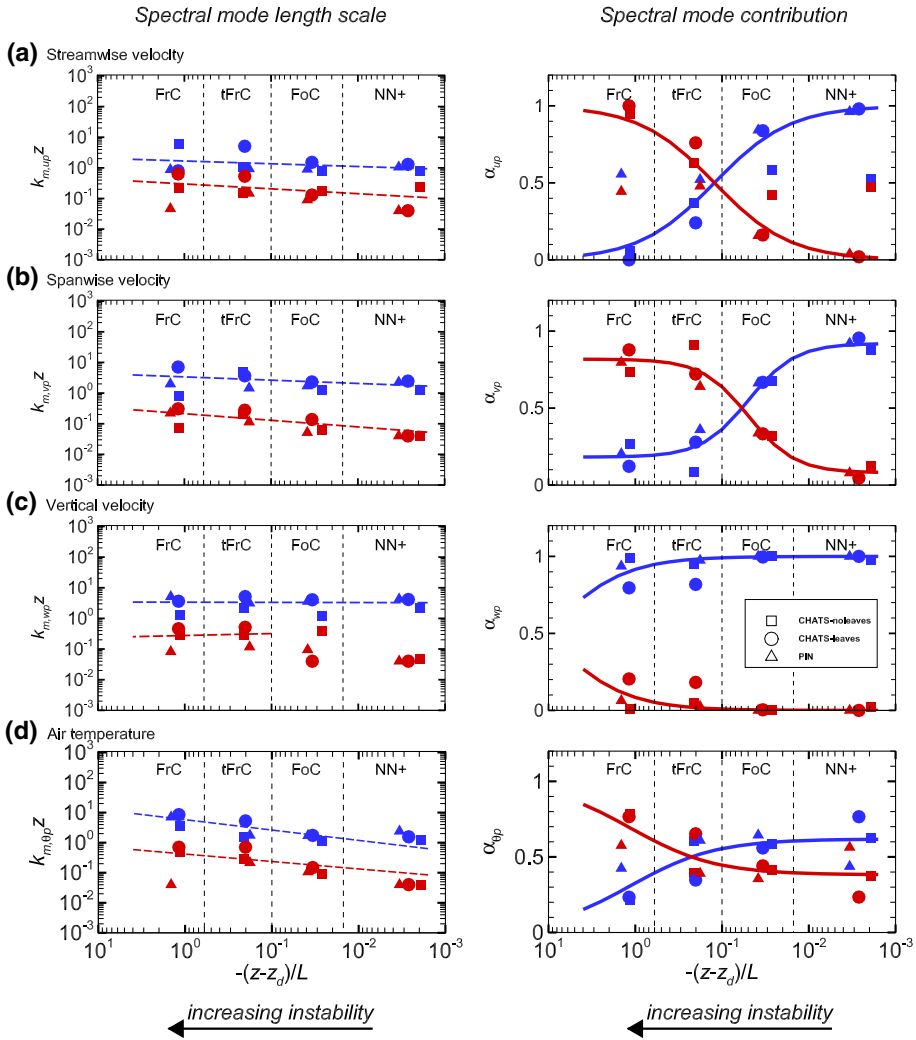


Fig. 8 Same as Fig. 7 but at canopy top for the RSL flows (CHATS-noleaves, CHATS-leaves and PIN experiments), where all spectra were decomposed with just two spectral modes [$p = 1$ (red) and 2 (blue)]

Contributions from the large-scale modes to w - and θ -spectra ($p = 1$) also increase but mainly in the FrC regime [$-(z - z_d)/L > 0.6$]. For this last regime, u - and v -spectra appear totally dominated by the largest-scale mode, while the large-scale mode contributes only 75% of the θ -spectrum and 50% of the w -spectrum.

In RSL flows under near-neutral conditions (NN+), the three velocity spectra are dominated by canopy-scale motions (highest-wavenumber mode, $p = 2$), with a negligible contribution from the large-scale mode ($p = 1$), which is consistent with the absence of a plateau in the u - and v -spectra. The θ -spectrum is also dominated by canopy-scale motions but in a lower proportion. With increasing instability, the contribution from the large-scale mode increases and becomes dominant for u - and θ -spectra at $-(z - z_d)/L > 0.2$ (tFrC regime) and for v -spectra at $-(z - z_d)/L > 0.06$ (FoC regime), while for w -spectra the

large-scale mode becomes only significant ($> 10\%$) in the FrC regime [$-(z - z_d)/L > 1.0$], but without dominating the canopy-scale mode. This transition of the spectral mode contribution with increasing influence of buoyancy is consistent with the levelling-off of the slope of the velocity spectra in the energy-containing subrange.

4.4 Momentum and Heat-Flux Cospectra

Similar to Figs. 3 and 4, Figs. 9 and 10 present the ensemble-averaged momentum and heat flux cospectra for WIND-O-V17 (ESL flow) and CHATS (RSL flow) experiments. Cospectra from the other experiments are presented in Online Resource Figs. S7–S9.

For windy conditions (NN+ and NN–), the uw -cospectra exhibit a well-defined peak, which peaks for the RSL flows at a scale intermediate between the u - and w -spectral peaks, and for the ESL flows at a scale intermediate between the high-wavenumber side of the plateau in the u -spectrum and of the w -spectral peak. The ESL uw -cospectral peak around $kz = 0.3$ for all measurement heights, suggesting that momentum is mainly transported by eddies corresponding to the intermediate spectral mode of the u -spectra ($p = 2$). In contrast, the RSL uw -cospectral peaks shift toward lower wavenumbers with increasing height above the canopy, decreasing from $kz = 3$ at canopy top to 1 at $z = 2.9h$ for the CHATS-leaves experiment. This shift of the above-canopy uw -cospectral peak with height may reflect a progressive transitioning from RSL flow near the canopy top to ISL flow further above at $z = 2.9h$. At the canopy top, momentum appears to be transported primarily by canopy-scale eddies (the highest-wavenumber spectral mode, $p = 2$). For both ESL and RSL flows, eddies appear inactive at transporting momentum at high and low wavenumbers. At high wavenumbers, this is explained by the eddies being of insufficient size to interact with the absorbing surface (detached eddies), and at low wavenumbers, by the insufficient amplitude of the vertical velocity fluctuations associated with the impinging ABL-scale motions to vertically transfer momentum. The $w\theta$ -cospectra have similar shape as the $-uw$ -cospectra, with a similar shift of the RSL cospectral peaks to lower wavenumbers with increasing height. However, the entire $w\theta$ -cospectra appear slightly shifted toward higher wavenumbers in ESL flows, reflecting better transport efficiency of heat than momentum by the small scale eddies as previously observed by Kaimal et al. (1972), and conversely a higher transport efficiency of momentum by large scale eddies.

For low wind conditions (free convection and stable regimes), the uw -cospectra show erratic fluctuations at low frequencies. Note that extreme fluctuations have been removed from the plots as indicated by the hatched areas. Interestingly, the ESL uw -cospectral peak shifts slightly toward higher wavenumbers in the FrC regime, coinciding with the $w\theta$ -cospectral peaks. This suggests that buoyantly-driven motions increasingly transport momentum at small scales. For both ESL and RSL flows under free-convective conditions, heat transport by low-wavenumber eddies does not appear to be enhanced compared to near-neutral conditions. In stable regimes, the $w\theta$ -cospectra show erratic fluctuations at low wavenumbers.

5 Discussion and Conclusion

Our wavelet spectral analysis reveals how the ABL-scale motions impact the turbulence differently near rough surfaces (ESL flow) and at canopy top (RSL flow), and how this influence of ABL-scale motions evolves with the thermal stratification. We find significant similarities between our two rough-surface cases (bare soil and sparsely vegetated soil)

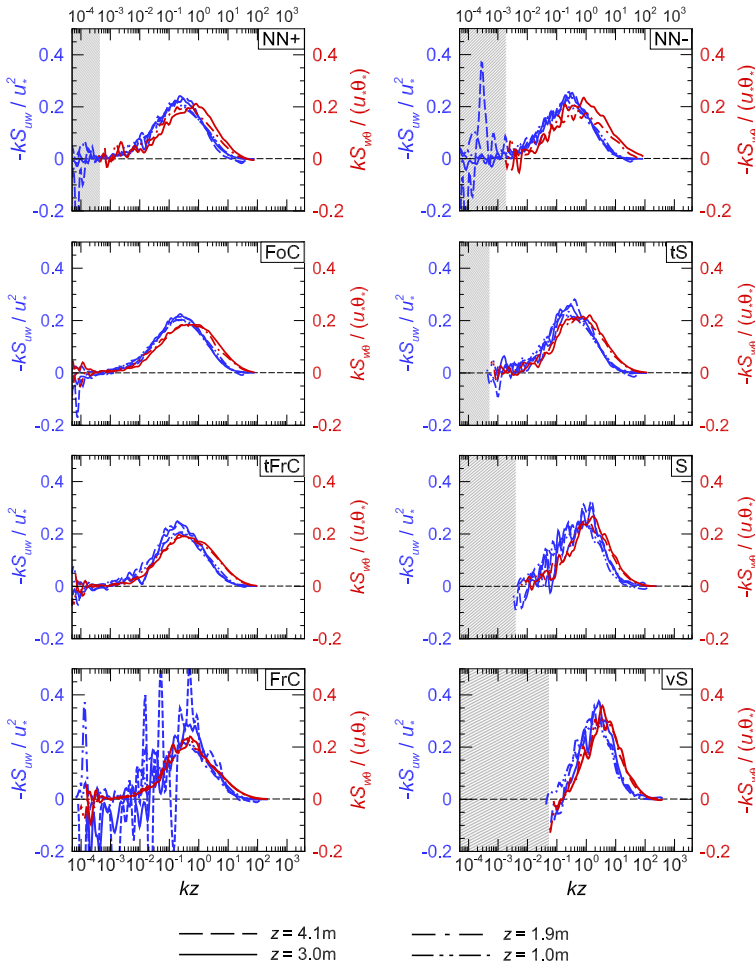


Fig. 9 Ensemble-averaged wavelet-based 30-min premultiplied cospectra of the momentum (S_{wv} , blue) and heat ($S_{w\theta}$, red) fluxes at the four measurement heights of the WIND-O-V17 experiment. The cospectra are normalized by the friction velocity (u_*) and the temperature scale ($\theta_* = |H|/u_*$). The wavenumber k was deduced as $k = 2\pi f/u$, where f is the frequency and u the mean wind speed at the measurement height, and was normalized by the measurement height z . Hatched areas indicate high erratic fluctuations for the missing cospectra in these areas of the plot. Heat-flux cospectra at 1.0 and 4.1 m heights were discarded because the former exhibited damped temperature fluctuations at high frequencies, and the latter had too many erratic values. Similarly, momentum-flux cospectra at 4.1 m heights in vS regimes were discarded because of too many erratic values. An equivalent figure for the WIND-O-V18 experiment is available in Online Resource Fig. S7

and between our three canopy cases (walnut trees without and with leaves, and maritime pine trees); this consistency of our findings for both ESL and RSL flows strengthens our conclusions.

In high wind conditions (NN-, NN+), the influence of ABL-scale motions on near-surface turbulence appears to be independent of the sign of the heat flux because the turbulence is primarily shear-driven. More importantly, ESL flows exhibit stronger influence of ABL-scale motions than do RSL flows. This is inferred from the plateau of the ESL premultiplied u - and

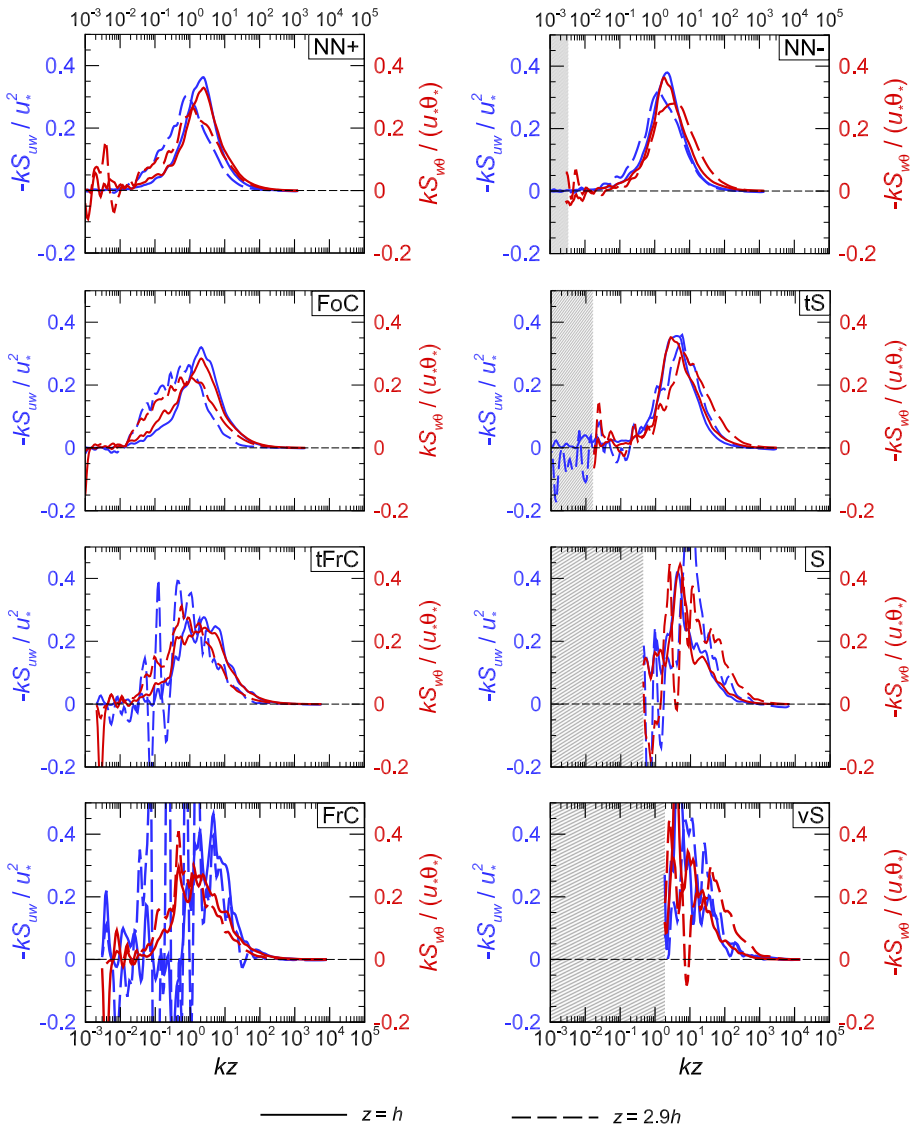


Fig. 10 Ensemble-averaged wavelet-based 30-min premultiplied cospectra of the momentum (S_{uw}) and heat ($S_{w\theta}$) fluxes for the CHATS-leaves experiment at canopy top and at $z = 2.9h$. The cospectra are normalized by the friction velocity (u_*) and the temperature scale ($\theta_* = |H|/u_*$). The wavenumber k was deduced as $k = 2\pi f/u$, where f is the frequency and u the mean wind speed at the measurement height, and was normalized by the measurement height z . Hatched areas indicate high erratic fluctuations for the missing cospectra in these areas of the plot. Equivalent figures for the CHATS-noleaves and PIN experiments are available in Online Resource Figs. S8–S9

v -spectra at mid-wavenumbers, corresponding to a k^{-1} scaling in non-premultiplied spectra, while RSL velocity spectra show a marked peak, flanked by k^{+1} and $k^{-2/3}$ scalings on the low- and high-wavenumber sides, respectively. This difference between ESL and RSL flows is further confirmed by the decomposition of the velocity spectra in spectral modes, showing a negligible contribution (less than 10%) of the large-scale mode on canopy-top velocity fluctuations while ESL velocity fluctuations are dominated by two large-scale modes, with the contribution from the local-scale mode representing only 12%.

In near-neutral conditions, the differences in behaviour between near-rough-surface and canopy-top wind spectra can be related to the coherent motions dominating ESL and RSL flows, respectively. The ESL flow is thought to be populated with packets of hairpin vortices (LSM) scaling with the ASL depth (see Sect. 2.4). Further above the surface, in the ISL, these packets may coalesce, forming VLMSs with longitudinal size larger than 10 times the ASL depth (e.g., Kim and Adrian 1999; Marusic and Hutchins 2008). Following the LES of Salesky and Anderson (2018), the low-wavenumber border of the k^{-1} scaling of the horizontal velocity spectra reflects the signature of VLMSs, while the high-wavenumber border of the k^{-1} scaling is associated to LSMs. We, therefore, suspect that the two large-scale modes emerging from the ESL horizontal velocity spectral decomposition correspond to LSMs (intermediate-scale mode, $p = 2$, corresponding to motions scaling around 100 m) and VLMSs (largest-scale mode, $p = 1$, corresponding to motions scaling around 1800 m). Very-large-scale-motions may scale with the ABL depth since they are somehow linked with the above mixed-layer convective rolls (see Sect. 2.4). Our spectral decomposition indicates that both scales of motion (LSM and VLMS) contribute almost equally to the ESL horizontal wind velocity variances.

The absence of a k^{-1} region in the horizontal velocity spectra of the RSL flow at $z = h$ is consistent with the LES results of Patton et al. (2016, their Fig. 8), but differs from Ghannam et al. (2018). However, the k^{-1} scaling in Ghannam et al. (2018) only extended over less than a decade. As previously discussed, the k^{-1} scaling may result from a bimodal spectral distribution associated to two motion scales, such as LSMs and VLMSs in ESL flows. The absence of k^{-1} scaling in canopy-top RSL flows does not mean that VLMSs are not present but it may suggest that either (1) their influence on the near-canopy turbulence is negligible and are overwhelmed by the turbulence resulting from the canopy-scale eddies generated by the inflection-point instability at canopy top, or (2) some of the energy transferred from the vertical to the horizontal velocity components due to surface blockage of the impinging large-scale motions (e.g., Hunt and Graham 1978) is absorbed by the canopy drag.

With increasing buoyancy, the influence of ABL-scale motions increases in both ESL and RSL flows. This is visible from (1) the progressive transitioning of both, the k^{-1} scaling of the ESL flows and the k^0 scaling of the RSL flows in near-neutral conditions, to a $k^{-5/3}$ scaling in FrC conditions for both flows, extending the inertial subrange to lower wavenumbers and shifting the production subrange to lower wavenumbers, and (2) the increasing contribution of the largest-scale spectral mode (Fig. 7), with ABL-scale motions reaching a peak contribution to near-surface u - and v -variances of more than 70% in FrC conditions. Similar sensitivity to increasing influence of buoyancy on the velocity spectra was observed by Banerjee et al. (2015) above a fallow land (ESL flow), and was simulated by Patton et al. (2016) over a vegetation canopy (RSL flow). Our spectral decomposition demonstrates that with increasing instability, the transition to 70% contribution by the ABL-scale motions in u - and v -spectra occurs in the tFrC regime. Interestingly, this transition is also accompanied (1) by an increase of the w skewness (Sk_w) from negative to near-zero values in RSL flows and from negative to positive values in ESL flows (Fig. 3c), and (2) by a decrease of the momentum correlation coefficient $-r_{uw}$ (Fig. 3d). Both behaviours reflect, respectively, (1) the increasing importance

of intermittent rising buoyant plumes emanating from the underlying ground surface or the vegetation canopy on the w -fluctuations, and (2) the progressive decrease of the spatial area where momentum sweep and ejection motions transport momentum. For w -spectra, the influence of LSMs only becomes significant for $-(z - z_d)/L > 0.6$ (FrC regime) but with a contribution remaining lower than 60% in ESL flows and lower than 20% in RSL flows.

In terms of coherent motions, we suspect that the progressive transition from k^{-1} to $k^{-5/3}$ scaling of the horizontal velocity spectra in ESL flows with increasing instability reflects an evolution of ABL convective rolls with VLMS underneath (Fig. 1a), to ABL-scale thermals (Fig. 1b, c), and a disappearance of VLMSs, as observed by Salesky and Anderson (2018) from their LES. In RSL flows, the coherent motions evolve from dominant shear-driven canopy-scale eddies to a combination of both shear- and buoyantly-driven eddies. With increasing instability, the canopy-scale eddies become less energetic as the wind shear decreases, accentuating the influence of velocity fluctuations associated with ABL-scale motions generated by surface blocking. At canopy top, these ABL-scale motions produce both local regions of convergence/divergence with weak shear, and local regions between the convergence/divergence with stronger wind shear (Patton et al. 2016). Hence, in free convection, ABL-scale thermals become the main source of u - and v -fluctuations near the surface and at canopy top, with spatially-varying contributions from shear versus buoyancy controlled by position relative to the ABL-scale convective cells (Fig. 1c).

With increasing stability, ESL and RSL turbulence can decouple from the overhead motions; an interpretation supported by the shift of the spectral gap in horizontal wind spectra from mid to higher wavenumbers with increasing stability and the emergence of a gap at similar wavenumbers in the vertical wind spectra. McNaughton and Laubach (2000) noted similar decoupling above a paddy field downwind of an extensive dry region (corresponding to a turbulent stable layer beneath a convective layer), as did Cheynet et al. (2018) above the sea surface. This decoupling is first visible in the tS regime in the v -spectra, suggesting that impingement of downwelling ABL-scale motions onto a near-surface weakly-stable layer leads to near-surface motions biased in the mean wind direction.

Similar to the u - and v -spectra in the ESL, air temperature spectra in the ESL exhibit a k^{-1} scaling at mid wavenumbers under windy and light heat flux conditions (FoC), which also suggests an influence of ABL-scale motions. This k^{-1} scaling vanishes with increasing instability as observed by Li et al. (2016) above a lake and a grass field. However, unlike the u - and v -spectra, the k^{-1} scaling in the θ -spectra is not replaced by an extension of the inertial subrange. Instead, the θ -spectral peak remains intermediate between the peak of the u - and w -spectra. Consequently, the local-scale mode contributes more to the θ -spectra than it does to the u - and v -spectra but less than it contributes to w -spectra. In RSL flows, the θ -spectra resemble the u -spectra. The contribution of ABL-scale motions increases with instability but remains lower than for the u - and v -spectra. In both ESL and RSL flows, u - and v -spectra show a clear inertial subrange, but θ -spectra do not, however θ -spectra exhibit an amplitude increase at mid- to high-wavenumbers. This absence of a well-defined inertial subrange was also observed by Li et al. (2016) and this could either result from the spatial attenuation of θ -fluctuations at high wavenumbers due to path-averaging between the sonic anemometer transducers (Horst and Oncley 2006), or indicate that the production of temperature fluctuations occurs over a large range of scales. In this latter case, the difference in the spectral range producing fluctuations in u - and θ -spectra may reflect the different spatial locations and motions producing u and θ fluctuations. Near-surface u fluctuations are more likely produced between the regions of large-scale divergence and convergence, while θ fluctuations are more likely produced beneath the large-scale downdrafts and updrafts (within the divergence and convergence regions produced by the ABL-scale structures). Additionally,

positive fluctuations of θ likely result from the continuous coalescence in scale of buoyantly-rising plumes, forming the large-scale updrafts (which implies a bottom-up process), which may explain the curvature of the θ -spectra at high wavenumbers.

Near-surface turbulent transport of momentum and heat by ABL-scale motions (VLSMs or thermals) is found to generally be negligible for both ESL and RSL flows, a result deduced from the small energy of uw - and $w\theta$ -cospectra at low and mid wavenumbers. However, LSMs in ESL flows contribute significantly in momentum transport, which is consistent with Ganapathisubramani et al. (2003). In RSL flows, canopy-scale eddies drive turbulent fluxes, which means that the ‘envelope’ of ABL-scale motions does not transport momentum or heat on average. ABL-scale motions may intermittently or locally transport momentum or heat vertically, but on average this transport seems negligible. The near-surface vertical velocity component of these large-scale motions is too small to induce significant vertical transport. However, ABL-scale motions may spatially organize (or modulate) near-surface turbulent transport by local-scale motions as demonstrated from LES by Salesky and Anderson (2018) and Li et al. (2018) above rough surfaces and by Patton et al. (2016) and Perret and Patton (2021) at canopy top.

In the upper RSL and close to the ISL ($z = 2.9h$ in the CHATS experiments), the horizontal velocity spectra exhibit a scaling intermediate between the k^{+0} scaling at canopy top and the k^{-1} scaling of the ESL flow. This indicates that ABL-scale motions contribute more to the horizontal velocity variance in the upper RSL than at canopy top but this contribution is still lower than from the locally-produced eddies; a finding which further suggests that surface blocking of ABL-scale motions is felt less at more elevated heights in RSL flows than in ESL flows. These results are in line with the suggestion of Nickels et al. (2005) that the existence of the k^{-1} scaling depends on the measurement height relative to the surface roughness and boundary-layer depth, where the measurement height modulates the distance in wavenumber between the local and large-scale eddies.

To conclude, our results show a difference in the spectral range of the motions involved in the horizontal wind velocity turbulence between ESL and RSL flows in near-neutral stratification, with larger contributions from ABL-scale motions in ESL flows. The difference between ESL and RSL flows and the respective spectral range of the contributing motions, diminishes with increasing instability as ABL-scale motions dominate the velocity fluctuations in both flows. ABL-scale motions contribute little to fluxes of momentum and heat in the ESL and RSL, however, ABL-scale motions are involved in spatially organizing local motions actively performing the transport. The increasing contributions of ABL-scale motions with increasing instability on near-surface turbulence is consistent with our current knowledge of coherent motions populating the ABL and their modification with thermal stratification. Interestingly, the velocity and air temperature spectra appear well approximated by a linear superposition of individual spectra associated with the primary eddy scales comprising the flow, with contributions that vary according to the thermal stratification. Overall, our results suggest a need to account for ABL-scale motions in near-surface turbulence similarity theory (MOST).

Supplementary Information The online version contains supplementary material available at <https://doi.org/10.1007/s10546-022-00710-z>.

Acknowledgements We acknowledge the support of the French National Research Agency (ANR) under the grant ANR-15-CE02-0013 (project WIND-O-V). This material is based upon work supported by the National Center for Atmospheric Research, which is a major facility sponsored by the National Science Foundation under Cooperative Agreement No. 1852977. EGP was supported by a combination of NCAR’s: (1) Meoscale and Microscale Meteorology Laboratory, and (2) Geophysical Turbulence Program. The CHATS data were

provided by NCAR/EOL under the sponsorship of the National Science Foundation. The WIND-O-V and PIN data are available from the corresponding author on reasonable request. Finally, the authors thank three anonymous reviewers for their helpful comments.

References

- Adrian RJ (2007) Hairpin vortex organization in wall turbulence. *Phys Fluids* 19(041):301. <https://doi.org/10.1063/1.2717527>
- Angevine WM, Edwards JM, Lothon M, LeMone MA, Osborne SR (2020) Transition periods in the diurnally-varying atmospheric boundary layer over land. *Boundary-Layer Meteorol* 177:205–223. <https://doi.org/10.1007/s10546-020-00515-y>
- Antonia RA, Raupach MR (1993) Spectral scaling in a high Reynolds number laboratory boundary layer. *Boundary-Layer Meteorol* 65:289–306. <https://doi.org/10.1007/bf00705531>
- Atkinson BW, Zhang JW (1996) Mesoscale shallow convection in the atmosphere. *Rev Geophys* 34(4):403–431. <https://doi.org/10.1029/96rg02623>
- Baars WJ, Talluru KM, Hutchins N, Marusic I (2015) Wavelet analysis of wall turbulence to study large-scale modulation of small scales. *Exp Fluids* 56(10):188. <https://doi.org/10.1007/s00348-015-2058-8>
- Bailey BN, Stoll R (2016) The creation and evolution of coherent structures in plant canopy flows and their role in turbulent transport. *J Fluid Mech* 789:425–460. <https://doi.org/10.1017/jfm.2015.749>
- Banerjee T, Katul GG, Salesky ST (2015) Revisiting the formulations for the longitudinal velocity variance in the unstable atmospheric surface layer. *Q J R Meteorol Soc* 141(690, A):1699–1711. <https://doi.org/10.1002/qj.2472>
- Bradshaw P (1967) ‘Inactive’ motion and pressure fluctuations in turbulent boundary layers. *J Fluid Mech* 30(2):241–258. <https://doi.org/10.1017/s0022112067001417>
- Bradshaw P (1978) Comments on “horizontal velocity spectra in an unstable surface layer”. *J Atmos Sci* 35:1768–1769. [https://doi.org/10.1175/1520-0469\(1978\)035<1768:covsia>2.0.co;2](https://doi.org/10.1175/1520-0469(1978)035<1768:covsia>2.0.co;2)
- Brasseur JG, Wei C (1994) Interscale dynamics and local isotropy in high Reynolds number turbulence within triadic interactions. *Phys Fluid* 6(2):842–870. <https://doi.org/10.1063/1.868322>
- Calaf M, Hultmark M, Oldroyd HJ, Simeonov V, Parlange MB (2013) Coherent structures and the k^{-1} spectral behaviour. *Phys Fluid*. <https://doi.org/10.1063/1.4834436>
- Chamecki M, Dias NL, Salesky ST, Pan Y (2017) Scaling laws for the longitudinal structure function in the atmospheric surface layer. *J Atmos Sci* 74(4):1127–1147. <https://doi.org/10.1175/jas-d-16-0228.1>
- Cheynet E, Jakobsen JB, Reuder J (2018) Velocity spectra and coherence estimates in the marine atmospheric boundary layer. *Boundary-Layer Meteorol* 169:429–460. <https://doi.org/10.1007/s10546-018-0382-2>
- Darbieu C, Lohou F, Lothon M, de Arellano JVG, Couvreur F, Durand P, Pino D, Patton EG, Nilsson E, Blay-Carreras E, Gioli B (2015) Turbulence vertical structure of the boundary layer during the afternoon transition. *Atmos Chem Phys* 15(17):10,071–10,086. <https://doi.org/10.5194/acp-15-10071-2015>
- Deardorff JW (1972) Numerical investigation of neutral and unstable planetary boundary layer. *J Atmos Sci* 29:91–115. [https://doi.org/10.1175/1520-0469\(1972\)029<0091:nionau>2.0.co;2](https://doi.org/10.1175/1520-0469(1972)029<0091:nionau>2.0.co;2)
- Denmead OT, Bradley EF (1987) On scalar transport in plant canopies. *Irrig Sci* 8:131–149. <https://doi.org/10.1007/bf00259477>
- Domingues MO, Mendes O Jr, da Costa AM (2005) On wavelet techniques in atmospheric sciences. *Adv Space Res* 35:831–842. <https://doi.org/10.1016/j.asr.2005.02.097>
- Drobinski P, Carlotti P, Newsom RK, Banta RM, Foster RC, Redelsperger JL (2004) The structure of the near-neutral atmospheric surface layer. *J Atmos Sci* 61:699–714. [https://doi.org/10.1175/1520-0469\(2004\)061<0699:tsoatna>2.0.co;2](https://doi.org/10.1175/1520-0469(2004)061<0699:tsoatna>2.0.co;2)
- Dupont S (2020) Scaling of dust flux with friction velocity: time resolution effects. *J Geophys Res Atmos*. <https://doi.org/10.1029/2019jd031192>
- Dupont S, Patton EG (2012a) Influence of stability and seasonal canopy changes on micrometeorology within and above an orchard canopy: the chats experiment. *Agric For Meteorol* 157:11–29. <https://doi.org/10.1016/j.agrformet.2012.01.011>
- Dupont S, Patton EG (2012b) Momentum and scalar transport within a vegetation canopy following atmospheric stability and seasonal canopy changes: the CHATS experiment. *Atmos Chem Phys* 12:5913–5935. <https://doi.org/10.5194/acp-12-5913-2012>
- Dupont S, Rajot JL, Labiadh M, Bergametti G, Alfaro S, Bouet C, Fernandes R, Khalfallah B, Lamaud E, Marticorena B, Bonnefond JM, Chevaillier S, Garrigou D, Henry-des-Tureaux T, Sekrafi S, Zapf P (2018) Aerodynamic parameters over an eroding bare surface: reconciliation of the Law-of-the-wall and Eddy-Covariance determinations. *J Geophys Res* 123:4490–4508. <https://doi.org/10.1029/2017jd027984>

- Dupont S, Rajot JL, Labiadh M, Bergametti G, Lamaud E, Irvine M, Alfaro S, Bouet C, Fernandes R, Khalfallah B, Marticorena B, Bonnefond JM, Chevaillier S, Garrigou D, Henry-des-Tureaux T, Sekrafi S, Zapf P (2019) Dissimilarity between dust, heat, and momentum turbulent transports during aeolian soil erosion. *J Geophys Res*. <https://doi.org/10.1029/2018jd029048>
- Dupont S, Argoul F, Gerasimova-Chechkina E, Irvine MR, Arneodo A (2020) Experimental evidence of a phase transition in the multifractal spectra of turbulent temperature fluctuations at a forest canopy top. *J Fluid Mech* 896:A15. <https://doi.org/10.1017/jfm.2020.348>
- Fesquet C, Dupont S, Drobinski P, Dubos T, Barthlott C (2009) Impact of terrain heterogeneity on coherent structure properties: numerical approach. *Boundary-Layer Meteorol* 133:71–92. <https://doi.org/10.1007/s10546-009-9412-4>
- Finnigan JJ, Shaw RH, Patton EG (2009) Turbulence structure above a vegetation canopy. *J Fluid Mech* 637:387–424. <https://doi.org/10.1017/s0022112009990589>
- Ganapathisubramani B, Longmire E, Marusic I (2003) Characteristics of vortex packets in turbulent boundary layers. *J Fluid Mech* 478:35–46. <https://doi.org/10.1017/s0022112002003270>
- Gao Z, Liu H, Russell ES, Huang J, Foken T, Oncley SP (2016) Large eddies modulating flux convergence and divergence in a disturbed unstable atmospheric surface layer. *J Geophys Atmos* 121(4):1475–1492. <https://doi.org/10.1002/2015jd024529>
- Gerz T, Howell J, Mahrt L (1994) Vortex structures and microfronts. *Phys Fluids* 6(3):1242–1251. <https://doi.org/10.1063/1.868293>
- Ghannam K, Katul GG, Bou-Zeid E, Gerken T, Chamecki M (2018) Scaling and similarity of the anisotropic coherent eddies in near-surface atmospheric turbulence. *J Atmos Sci* 75:943–964. <https://doi.org/10.1175/jas-d-17-0246.1>
- Guala M, Hommema S, Adrian R (2006) Large-scale and very-large-scale motions in turbulent pipe flow. *J Fluid Mech* 554:521–542. <https://doi.org/10.1017/s0022112006008871>
- Harman IN, Finnigan JJ (2007) A simple unified theory for flow in the canopy and roughness sublayer. *Boundary-Layer Meteorol* 123:339–363. <https://doi.org/10.1007/s10546-006-9145-6>
- Harman IN, Finnigan JJ (2008) Scalar concentration profiles in the canopy and roughness sublayer. *Boundary-Layer Meteorol* 129:323–351. <https://doi.org/10.1007/s10546-008-9328-4>
- Heisenberg W (1948) On the theory of statistical and isotropic turbulence. *Proc R Soc Lond* 195:402–406. https://doi.org/10.1007/978-3-642-61659-4_8
- Högström U, Hunt J, Smedman A (2002) Theory and measurements for turbulence spectra and variances in the atmospheric neutral surface layer. *Boundary-Layer Meteorol* 103(1):101–124. <https://doi.org/10.1023/a:1014579828712>
- Højstrup J (1982) Velocity spectra in the unstable planetary boundary-layer. *J Atmos Sci* 39(10):2239–2248. [https://doi.org/10.1175/1520-0469\(1982\)039<2239:vsitup>2.0.co;2](https://doi.org/10.1175/1520-0469(1982)039<2239:vsitup>2.0.co;2)
- Horst T (2019) NCAR/EOL ISFS CHATS high rate tower and array data. Version 2. <https://doi.org/10.26023/P4JW-9T0T-QG0S>
- Horst TW, Oncley SP (2006) Corrections to inertial-range power spectra measured by CSAT3 and solent sonic anemometers, 1. Path-averaging errors. *Boundary-Layer Meteorol* 119:375–395. <https://doi.org/10.1007/s10546-005-9015-7>
- Hunt JCR, Graham JMR (1978) Free-stream turbulence near plane boundaries. *J Fluid Mech* 84:209–235. <https://doi.org/10.1017/s0022112078000130>
- Hunt J, Morrison JF (2000) Eddy structure in turbulent boundary layers. *Euro J Mech B Fluids* 19:673–694. [https://doi.org/10.1016/s0997-7546\(00\)00129-1](https://doi.org/10.1016/s0997-7546(00)00129-1)
- Hunt J, Carlotto P (2001) Statistical structure at the wall of the high Reynolds number turbulent boundary layer. *Flow Turb Comb* 66(4):453–475. <https://doi.org/10.1023/A:1013519021030>
- Hutchins N, Marusic I (2007) Evidence of very long meandering features in the logarithmic region of turbulent boundary layers. *J Fluid Mech* 579:1–28. <https://doi.org/10.1017/s0022112006003946>
- Jayaraman B, Brasseur JG (2021) Transition in atmospheric boundary layer turbulence structure from neutral to convective, and large-scale rolls. *J Fluid Mech* 913:A42. <https://doi.org/10.1017/jfm.2021.3>
- Kader BA, Yaglom AM (1991) Spectra and correlation functions of surface layer turbulence in unstable thermal stratification. In: *Turbulence and coherent structures*. Kluwer Academic Press, New York, pp 388–412. https://doi.org/10.1007/978-94-015-7904-9_24
- Kaimal JC (1978) Horizontal velocity spectra in an unstable surface layer. *J Atmos Sci* 35:18–24. [https://doi.org/10.1175/1520-0469\(1978\)035<0018:hvsiau>2.0.co;2](https://doi.org/10.1175/1520-0469(1978)035<0018:hvsiau>2.0.co;2)
- Kaimal JC, Finnigan JJ (1994) *Atmospheric boundary layer flows*. Their structure and measurements. Oxford University Press, New-York. <https://doi.org/10.1093/oso/9780195062397.001.0001>
- Kaimal JC, Wyngaard JC, Izumi Y, Coté OR (1972) Spectral characteristics of surface-layer turbulence. *Q J R Meteorol Soc* 98:563–589. <https://doi.org/10.1002/qj.49709841707>

- Kaimal JC, Wyngaard JC, Haugen DA, Coté OR, Izumi Y (1976) Turbulence structure in the convective boundary layer. *J Atmos Sci* 33:2152–2169. [https://doi.org/10.1175/1520-0469\(1976\)033<2152:tsitcb>2.0.co;2](https://doi.org/10.1175/1520-0469(1976)033<2152:tsitcb>2.0.co;2)
- Katul GG (2019) The anatomy of large-scale motion in atmospheric boundary layers. *J Fluid Mech* 858:1–4. <https://doi.org/10.1017/jfm.2018.731>
- Katul GG, Parlange MB (1994) On the active role of temperature in surface-layer turbulence. *J Atmos Sci* 51(15):2181–2195. [https://doi.org/10.1175/1520-0469\(1994\)051<2181:otarat>2.0.co;2](https://doi.org/10.1175/1520-0469(1994)051<2181:otarat>2.0.co;2)
- Katul GG, Parlange MB (1995) The spatial structure of turbulence at production wavenumbers using orthonormal wavelets. *Boundary-Layer Meteorol* 75:81–108. <https://doi.org/10.1007/bf00721045>
- Katul G, Chu C (1998) A theoretical and experimental investigation of energy-containing scales in the dynamic sublayer of boundary-layer flows. *Boundary-Layer Meteorol* 86(2):279–312. <https://doi.org/10.1023/a:1000657014845>
- Katul G, Chang W (1999) Principal length scales in second-order closure models for canopy turbulence. *J Appl Meteorol* 38:1631–1643. [https://doi.org/10.1175/1520-0450\(1999\)038<1631:plsiso>2.0.co;2](https://doi.org/10.1175/1520-0450(1999)038<1631:plsiso>2.0.co;2)
- Katul GG, Albertson JD, Hsieh CI, Conklin PS, Sigmon JT, Knoerr Parlange KR M B (1996) The “inactive” eddy motion and the large-scale turbulent pressure fluctuations in the dynamic sublayer. *J Atmos Sci* 53:2512–2524. [https://doi.org/10.1175/1520-0469\(1996\)053<2512:tematl>2.0.co;2](https://doi.org/10.1175/1520-0469(1996)053<2512:tematl>2.0.co;2)
- Katul GG, Porporato A, Nikora V (2012) Existence of k^{-1} power-law scaling in the equilibrium regions of wall-bounded turbulence explained by heisenberg’s eddy viscosity. *Phys Rev E* 86(066):311. <https://doi.org/10.1103/PhysRevE.86.066311>
- Khanna S, Brasseur JG (1997) Analysis of Monin–Obukhov similarity from large-eddy simulation. *J Fluid Mech* 345:251–286. <https://doi.org/10.1017/s0022112097006277>
- Khanna S, Brasseur JG (1998) Three-dimensional buoyancy- and shear-induced local structure of the atmospheric boundary layer. *J Atmos Sci* 55(5):710–743. [https://doi.org/10.1175/1520-0469\(1998\)055<0710:tdbasi>2.0.co;2](https://doi.org/10.1175/1520-0469(1998)055<0710:tdbasi>2.0.co;2)
- Kim KC, Adrian RJ (1999) Very large-scale motion in the outer layer. *Phys Fluids* 11(2):417–422. <https://doi.org/10.1063/1.869889>
- Larsen XG, Larsen SE, Petersen EL (2016) Full-scale spectrum of boundary-layer winds. *Boundary-Layer Meteorol* 159(2):349–371. <https://doi.org/10.1007/s10546-016-0129-x>
- Lee JH, Sung HJ (2011) Very-large-scale motions in a turbulent boundary layer. *J Fluid Mech* 673:80–120. <https://doi.org/10.1017/s002211201000621x>
- Lemone MA (1973) The structure and dynamics of horizontal roll vortices in the planetary boundary layer. *J Atmos Sci* 30:1077–1091. [https://doi.org/10.1175/1520-0469\(1973\)030<1077:tsadoh>2.0.co;2](https://doi.org/10.1175/1520-0469(1973)030<1077:tsadoh>2.0.co;2)
- Li D, Katul GG, Gentile P (2016) The k^{-1} scaling of air temperature spectra in atmospheric surface layer flows. *Q J R Meteorol Soc* 142(694, A):496–505. <https://doi.org/10.1002/qj.2668>
- Li Q, Gentile P, Mellado JP, McColl KA (2018) Implications of nonlocal transport and conditionally averaged statistics on Monin–Obukhov similarity theory and Townsend’s attached eddy hypothesis. *J Atmos Sci* 75(10):3403–3431. <https://doi.org/10.1175/jas-d-17-0301.1>
- Mahrt L (2014) Stably stratified atmospheric boundary layers. *Ann Rev Fluid Mech* 46:23–45. <https://doi.org/10.1146/annurev-fluid-010313-141354>
- Marusic I, Hutchins N (2008) Study of the log-layer structure in wall turbulence over a very large range of Reynolds number. *Flow Turb Comb* 81:115–130. <https://doi.org/10.1007/s10494-007-9116-0>
- Marusic I, Monty JP (2019) Attached eddy model of wall turbulence. *Annu Rev Fluid Mech* 51:49–74. <https://doi.org/10.1146/annurev-fluid-010518-040427>
- Mathis R, Hutchins N, Marusic I (2009) Large-scale amplitude modulation of the small scale structures in turbulent boundary layers. *J Fluid Mech* 628:311–337. <https://doi.org/10.1017/s0022112009006946>
- McNaughton K (2004) Turbulence structure of the unstable atmospheric surface layer and transition to the outer layer. *Boundary-Layer Meteorol* 112(2):199–221. <https://doi.org/10.1023/b:boun.0000027906.28627.49>
- McNaughton K, Laubach J (2000) Power spectra and cospectra for wind and scalars in a disturbed surface layer at the base of an advective inversion. *Boundary-Layer Meteorol* 96(1–2):143–185. <https://doi.org/10.1023/a:1002477120507>
- McNaughton KG, Clement RJ, Moncrieff JB (2007) Scaling properties of velocity and temperature spectra above the surface friction layer in a convective atmospheric boundary layer. *Nonlinear Process Geophys* 14(3):257–271. <https://doi.org/10.5194/npg-14-257-2007>
- Mikkelsen T, Larsen SE, Jørgensen HE, Astrup P, Larsen XG (2017) Scaling of turbulence spectra measured in strong shear flow near the Earth’s surface. *Phys Scr*. <https://doi.org/10.1088/1402-4896/aa91b2>
- Moeng CH, Sullivan PP (1994) Comparison of shear- and buoyancy-driven planetary boundary layer flows. *J Atmos Sci* 51:999–1022. [https://doi.org/10.1175/1520-0469\(1994\)051<0999:acosab>2.0.co;2](https://doi.org/10.1175/1520-0469(1994)051<0999:acosab>2.0.co;2)

- Monin AS, Obukhov AMF (1954) Basic laws of turbulent mixing in the surface layer of the atmosphere. *Tr Akad Nauk SSSR Geophys* 24(151):163–187
- Morrison JF, Jiang W, McKeon BJ, Smits AJ (2002) Reynolds number dependence of streamwise velocity spectra in turbulent pipe flow. *Phys Rev Lett* 88(21):214,501. <https://doi.org/10.1103/physrevlett.88.214501>
- Nickels T, Marusic I, Hafez S, Chong M (2005) Evidence of the k^{-1} law in a high-Reynolds-number turbulent boundary layer. *Phys Rev Lett*. <https://doi.org/10.1103/PhysRevLett.95.074501>
- Nikora V (1999) Origin of the “-1” spectral law in wall-bounded turbulence. *Phys Rev Lett* 83(4):734–736. <https://doi.org/10.1103/PhysRevLett.83.734>
- Obukhov AM (1946) Turbulence in an atmosphere with a non-uniform temperature. *Tr Inst Teor Geofiz Akad Nauk SSSR* 1:95–115. <https://doi.org/10.1007/bf00718085>
- Pan Y, Chamecki M (2016) A scaling law for the shear-production range of second-order structure functions. *J Fluid Mech* 801:459–474. <https://doi.org/10.1017/jfm.2016.427>
- Patton EG, Horst TW, Sullivan PP, Lenschow DH, Oncley SP, Brown OJ, Burns SP, Guenther AB, Held A, Karl T, Mayor SD, Rizzo LV, Spuler SM, Sun J, Turnipseed A, Allwine EJ, Edburg SL, Avissar Lamb R B K, Calhoun RJ, Kleissl J, Massman WJ, Paw UKT, Weil JC (2011) The canopy horizontal array turbulence study. *Bull Am Meteorol Soc* 92:593–611. <https://doi.org/10.1175/2010bams2614.1>
- Patton EG, Sullivan PP, Shaw RH, Finnigan JJ, Weil JC (2016) Atmospheric stability influences on coupled boundary layer and canopy turbulence. *J Atmos Sci* 73(4):1621–1647. <https://doi.org/10.1175/jas-d-15-0068.1>
- Perret L, Patton EG (2021) Stability influences on interscale transport of turbulent kinetic energy and Reynolds shear stress in atmospheric boundary layers interacting with a tall vegetation canopy. *J Fluid Mech* 921:A14. <https://doi.org/10.1017/jfm.2021.453>
- Perry AE, Henbest S, Chong MS (1986) A theoretical and experimental study of wall turbulence. *J Fluid Mech* 165:163–199. <https://doi.org/10.1017/s002211208600304x>
- Raupach MR, Antonia RA, Rajagopalan S (1991) Rough wall turbulent boundary layers. *Appl Mech Rev* 44:1–25. <https://doi.org/10.1115/1.3119492>
- Raupach MR, Finnigan JJ, Brunet Y (1996) Coherent eddies and turbulence in vegetation canopies: The mixing-layer analogy. *Boundary-Layer Meteorol* 78(3–4):351–382. https://doi.org/10.1007/978-94-017-0944-6_15
- Reynolds RT, Hayden P, Castro IP, Robins AG (2007) Spanwise variations in nominally two-dimensional rough-wall boundary layers. *Exp Fluids* 42(2):311–320. <https://doi.org/10.1007/s00348-006-0243-5>
- Salesky ST, Chamecki M (2012) Random errors in turbulence measurements in the atmospheric surface layer: Implications for Monin-Obukhov similarity theory. *J Atmos Sci* 69:3700–3714. <https://doi.org/10.1175/jas-d-12-096.1>
- Salesky ST, Anderson W (2018) Buoyancy effects on large-scale motions in convective atmospheric boundary layers: implications for modulation of near-wall processes. *J Fluid Mech* 856:135–168. <https://doi.org/10.1017/jfm.2018.711>
- Salesky ST, Chamecki M, Bou-Zeid E (2017) On the nature of the transition between roll and cellular organization in the convective boundary layer. *Boundary-Layer Meteorol* 163(1):41–68. <https://doi.org/10.1007/s10546-016-0220-3>
- Schaller C, Göckede M, Foken T (2017) Flux calculation of short turbulent events—comparison of three methods. *Atmos Meas Tech* 10:869–880. <https://doi.org/10.5194/amt-10-869-2017>
- Shapkalijevski M, Moene AF, Ouwersloot HG, Patton EG, Vila-Guerau de Arellano J (2016) Influence of canopy seasonal changes on turbulence parameterization within the roughness sublayer over an orchard canopy. *J Appl Meteorol Clim* 55:1391–1407. <https://doi.org/10.1175/jamc-d-15-0205.1>
- Shaw RH, Brunet Y, Finnigan JJ, Raupach MR (1995) A wind tunnel study of air flow in waving wheat: two-point velocity statistics. *Boundary-Layer Meteorol* 76(4):349–376. <https://doi.org/10.1007/bf00709238>
- Su HB, Schmid HP, Grimmond CSB, Vogel CS, Oliphant AJ (2004) Spectral characteristics and long-term eddy covariance measurements over two mixed hardwood forests in non-flat terrain. *Boundary-Layer Meteorol* 110:213–253. <https://doi.org/10.1023/A:1026099523505>
- Sullivan PP, Weil JC, Patton EG, Jonker HJJ, Mironov DV (2016) Turbulent winds and temperature fronts in large-eddy simulations of the stable atmospheric boundary layer. *J Atmos Sci* 73(4):1815–1840. <https://doi.org/10.1175/jas-d-15-0339.1>
- Tchen CM (1953) On the spectrum of energy in turbulent shear flow. *J Res Nat Bur Stand* 50:51–62. <https://doi.org/10.6028/jres.050.009>
- Tong C, Nguyen KX (2015) Multipoint Monin–Obukhov similarity and its application to turbulence spectra in the convective atmospheric surface layer. *J Atmos Sci* 72:4337–4348. <https://doi.org/10.1175/jas-d-15-0134.1>

- Torrence C, Compo GP (1998) A practical guide to wavelet analysis. *Bull Am Meteorol Soc* 79:61–78. [https://doi.org/10.1175/1520-0477\(1998\)079<0061:apgtwa>2.0.co;2](https://doi.org/10.1175/1520-0477(1998)079<0061:apgtwa>2.0.co;2)
- Townsend AA (1961) Equilibrium layers and wall turbulence. *J Fluid Mech* 11(1):97–120. <https://doi.org/10.1017/s0022112061000883>
- Vanderwel C, Ganapathisubramani B (2015) Effects of spanwise spacing on large-scale secondary flows in rough-wall turbulent boundary layers. *J Fluid Mech* 774:R2. <https://doi.org/10.1017/jfm.2015.292>
- van de Wiel BJH, Moene AF, Jonker HJJ, Baas P, Basu S, Donda JMM, Sun J, Holtslag AAM (2012) The minimum wind speed for sustainable turbulence in the nocturnal boundary layer. *J Atmos Sci* 69:3116–3127. <https://doi.org/10.1175/jas-d-12-0107.1>
- Weckwerth TM, Wilson JW, Wakimoto RM, Crook NA (1997) Horizontal convective rolls: Determining the environmental conditions supporting their existence and characteristics. *Mon Weather Rev* 125(4):505–526. [https://doi.org/10.1175/1520-0493\(1997\)125<0505:hcrdte>2.0.co;2](https://doi.org/10.1175/1520-0493(1997)125<0505:hcrdte>2.0.co;2)
- Weligepolage K, Gieske ASM, van der Tol C, Timmermans J, Su Z (2012) Effect of sub-layer corrections on the roughness parameterization of a douglas fir forest. *Agric For Meteorol* 162–163:115–126. <https://doi.org/10.1016/j.agrformet.2012.04.017>
- Wilczak JM, Tillman JE (1980) The three-dimensional structure of convection in the atmospheric surface layer. *J Atmos Sci* 37:2424–2443. [https://doi.org/10.1175/1520-0469\(1980\)037<2424:tdsoc>2.0.co;2](https://doi.org/10.1175/1520-0469(1980)037<2424:tdsoc>2.0.co;2)
- Wilczak JM, Oncley SP, Stage SA (2001) Sonic anemometer tilt correction algorithms. *Boundary-Layer Meteorol* 99(1):127–150. <https://doi.org/10.1023/a:1018966204465>
- Young GS, Kristovich DA, Hjelmfelt MR, Foster RC (2002) Rolls, streets, waves, and more: A review of quasi-two-dimensional structures in the atmospheric boundary layer. *Bull Am Meteorol Soc* 83(7):997–1002. <https://doi.org/10.1175/BAMS-83-7-Young>
- Zhang C, Shaw RH, Paw UKT (1992) Spatial characteristics of turbulent coherent structures within and above an orchard canopy. Precipitation scavenging and atmosphere-surface exchange. S. E. Schwartz and W. G. N. Slim, Richland, WA, pp 603–1172
- Zhang Y, Liu H, Foken T, Williams QL, Liu S, Mauder M, Liebethal C (2010) turbulence spectra and cospectra under the influence of large eddies in the Energy Balance EXperiment (EBEX). *Boundary-Layer Meteorol* 136(2):235–251. <https://doi.org/10.1007/s10546-010-9504-1>

Publisher's Note Springer Nature remains neutral with regard to jurisdictional claims in published maps and institutional affiliations.